Jorge André Pinto de Oliveira

Contamination sensor for an optical window

Contamination sensor for an optical window

Jorge André Pinto Oliveira

Uminho | 2021

Novembro de 2021
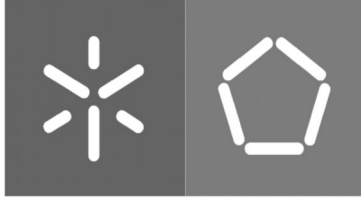
Universidade do Minho
Escola de Engenharia

Jorge André Pinto de Oliveira

Contamination sensor for an optical window

Dissertação de Mestrado
Engenharia Eletrónica Industrial e Computadores

Trabalho efetuado sob a orientação de
Professor Doutor Jorge Miguel Nunes dos Santos Cabral

Novembro de 2021

DIREITOS DE AUTOR E CONDIÇÕES DE UTILIZAÇÃO DO TRABALHO POR TERCEIROS

Este é um trabalho académico que pode ser utilizado por terceiros desde que respeitadas as regras e boas práticas internacionalmente aceites, no que concerne aos direitos de autor e direitos conexos. Assim, o presente trabalho pode ser utilizado nos termos previstos na licença abaixo indicada. Caso o utilizador necessite de permissão para poder fazer um uso do trabalho em condições não previstas no licenciamento indicado, deverá contactar o autor, através do RepositóriUM da Universidade do Minho.

STATEMENT OF INTEGRITY

I hereby declare having conducted this academic work with integrity. I confirm that I have not used plagiarism or any form of undue use of information or falsification of results along the process leading to its elaboration.

I further declare that I have fully acknowledged the Code of Ethical Conduct of the University of Minho.

Resumo

As condições climáticas e o seu efeito no piso são um fator com impacto significativo na condução de um veículo e na sua segurança. Por este motivo, a Bosch considera o Road Condition Sensor (RCS) como um dos sensores essenciais para permitir o advento de condução autónoma. O objetivo deste sensor é detetar a presença de água no solo, o seu estado, isto é, líquido, sob a forma de gelo ou neve, e a sua espessura.

O sensor reconhece as condições da superfície do piso iluminando a mesma com lasers de diferentes comprimentos de onda e analisando a intensidade de luz refletida. Devido à posição do sensor (próximo ao solo), uma das maiores ameaças é ser danificado ou contaminado com detritos e outros elementos. Para controlar esse risco e proteger o delicado hardware do sensor, uma janela de proteção é necessária para fazer uma barreira entre o RCS e os elementos externos.

Nesta dissertação, uma solução para reduzir e monitorizar a contaminação da janela de proteção é proposta. De maneira reduzir a contaminação, um revestimento com propriedades repelentes foi selecionado. Para verificar a contaminação presente na janela, um sensor que permite a deteção de contaminantes foi desenvolvido e testado. É baseado na propagação da luz por diferentes materiais. O sensor de deteção de contaminação explora o princípio de reflexão interna e identifica os contaminantes de acordo com a intensidade da luz perdida ou mantida dentro da janela.

Ao longo da dissertação, alguns efeitos óticos e propriedades foram medidos. A fim de caracterizar as propriedades espectrais dos revestimentos e contaminantes, um setup ótico envolvendo um *Optical Spectrum Analyzer* foi implementado. Com o uso de um *lock-in amplifier*, as perdas por *scattering* foram medidas.

O sensor de deteção de contaminação foi testado com diferentes revestimentos e, com um deles (aquele com maior capacidade de repulsão de contaminantes), o sensor pode identificar a presença de resíduos tal como água e diesel.

Abstract

The weather condition and its effect on the road surface are a factor with a significant impact on driving and driving safety. For this reason, Bosch regards the Road Condition Sensor (RCS) as one of the essential sensors to enable the advent of autonomous driving. The target of this sensor is to detect the presence of water in the road, its state (liquid, in the form of ice or snow) and its thickness.

The sensor recognizes the road surface conditions by illuminating the ground with lasers of different wavelengths and analyzing the reflected light intensity. Due to the sensor's position (near the ground), one of the biggest threats is getting damaged or contaminated with debris and other elements. To overcome this risk and protect the delicate sensor's hardware, a protection window is needed to make a barrier between the RCS and external elements.

In this dissertation, a solution to reduce and monitor the protection window contamination is proposed. To reduce contamination, a coating with repellent properties was selected. To monitor the contamination present in the window, a sensor that allows the detection of contaminants was developed and tested. It is based on light propagation through different materials. The contamination detection sensor explores the internal reflection principle and identifies the contaminants according to the intensity of light lost or kept inside the window.

Throughout the dissertation, some optical effects and properties were measured. In order to characterize the spectral properties of the coatings and contaminants, an optical setup involving an Optical Spectrum Analyzer was implemented. With the use of a lock-in amplifier, losses by scattering were measured.

The contamination detection sensor has been tested with different coatings and, with one of them (the one with the more repelling capability), the sensor can identify the presence of residues such as water and diesel.

Table of Contents

List of Figures

Chapter 1

Introduction

Self-driving vehicles represent one of the biggest challenges of the current era, where different engineering areas are working together to provide adequate solutions. Several technologies, usually developed by tech companies, are now being embraced by the automotive industry [1]. High computational effort is required for a vehicle to make the right decisions at the right time [2], and the decision-making system is a huge challenge by itself that requires artificial intelligence, secure and reliable architectures, connectivity, and positioning. However, the right decisions rely on having a sensory capacity that recreates the human perception. A vehicle has to be able to "see" at least similarly to a person, including identifying objects, obstacles, the lines on the ground, the condition of the weather and the road, and the ability to perceive depth or distances. The development of sensors that provide meaningful information about the vehicle's surroundings is a crucial step to self-driving technology [3].

1.1   Motivation

At this moment, there are some well-established technologies capable of acquiring information about the environment surrounding the vehicle. Since the currently available solutions do not provide enough reliable information, this is an area of constant improvement and research. The available solutions are excellent for their application, but human perception is extremely complex to mimic.

Ultrasonic sensors have been around for several years, exploring wave sound properties to measure the distance from obstacles (parking sensors) and detecting vehicles in blind spots. Nowadays, this type of sensor is massively implemented in vehicles; they present an excellent solution for detecting obstacles at close range. The principal limitations of ultrasonic sensors are their low resolution and their short range since sound waves cannot sustain their power for long distances [4].

With the interest of detecting obstacles at a greater distance than ultrasonic sensors, radar technology started being implemented in the automotive industry. Radar sensors use radio waves to detect obstacles and determine their distance. These sensors are commonly used in adaptive cruise control systems and autonomous driving assistance systems (ADAS). In adaptive cruise control, its function is to measure the distance to the vehicle in front and keep a safe gap. In ADAS, radar is used for collision avoidance, pedestrian and cyclist detection and complements vision-based camera-sensing systems [5].

More recently, optical sensors have been developed to evaluate the surroundings of vehicles. Like the sensors described above, LiDAR can identify the distance of obstacles and, besides that, it can reproduce 3D images with high resolution of the surroundings [6]. This type of information is a considerable aid in the decision-making process. Identifying objects and obstacles on the road is a crucial process for driving, although road condition also dictates how a vehicle is driven. A vehicle cannot behave equally on a dry or wet surface. Optical sensors can explore the spectral properties of different materials such as water to evaluate the road condition. This technique allows characterizing the surface beneath the vehicle: identify the presence of water, its state (liquid, in the form of ice or snow) and thickness.

Unlike other sensors, optical sensors present a new challenge: they are easily affected by contamination on the protective window. These contaminants can result in incorrect and misleading information [7]. The data provided by these sensors is only reliable if the condition of the window is monitored and controlled. With that in mind, a sensor capable of detecting this contamination is crucial for verifying that the optical sensor is providing accurate information to the decision making system.

1.2 Problem statement

This dissertation was developed within the *Sensible Car: Automated Driving* project. The project, a partnership between the University of Minho and Bosch, strives to develop smart sensors to respond to the requirements imposed by autonomous driving. The dissertation is framed in a development line of this project: the Road Condition Sensor. The Road Condition Sensor is one of those sensors whose end goal is characterizing the road surface conditions: identify the presence of water, its state (liquid, in the form of ice or snow) and thickness.

The Road Condition Sensor evaluates the surface condition by illuminating the ground with four lasers with different wavelengths and analyzing each reflection's intensity. The acquired intensities are fed to a classifier (artificial intelligence) that outputs the road condition (water presence and state). Since the RCS

is positioned on a vehicle and near the ground, it is highly vulnerable to getting damaged and contaminated with debris and other elements (such as liquid residues). To protect the delicate hardware that integrates the RCS, a protective window that separates the sensor from the outside elements is required. Considering that the working principle of the RCS depends on reflected light intensity, the window must not affect the RCS's performance and precision. A dirty window will lead to an improper operation if not adjusted by the identification algorithm or not cleaned. For this reason, a system capable of detecting contamination and maintaining the correct operation of the RCS must be implemented. The contamination detection sensor consists of monitoring the presence of contaminants on the surface of the protective window.
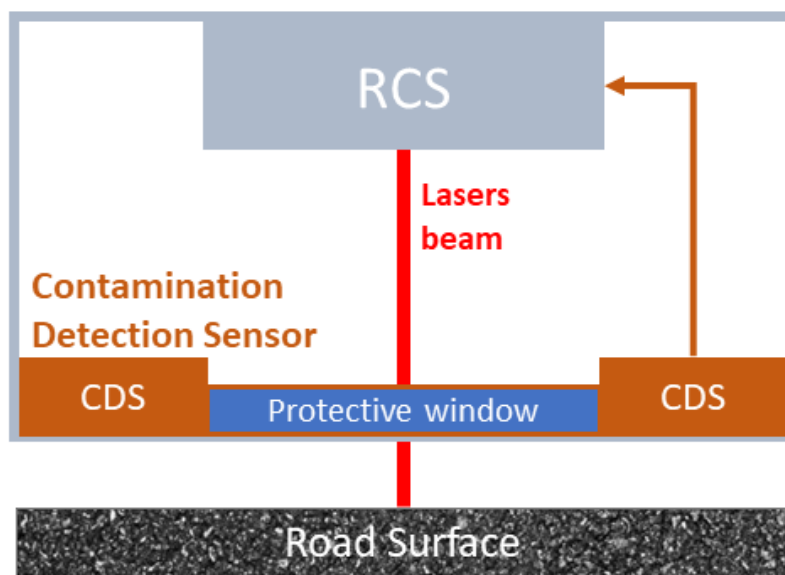
Figure 1.1: Location of Contamination Detection Sensor

1.3   Objectives

This dissertation proposes a solution to reduce and monitor the contamination of the protective window of the RCS. The main goals are to develop a sensor that allows to detect contaminants on the window, and to select a coating capable of repelling water, hydrocarbons and dirt, but simultaneously not interfering with the RCS normal operation.

1.4 Dissertation Structure

This dissertation is divided into five chapters. The first chapter provides an introduction and contextualization of the dissertation's theme.

Chapter 2 starts by covering the theoretical background that supports the operating principle of the contamination detection sensor. Essentially, the sensor's operating principle is based on light propagation through different materials. The relevant physical principles are presented throughout this chapter, as well as coating materials properties. Afterwards, technologies that explore similar operating principles are presented. Technologies like fiber optics and the automotive rain sensor are optical devices that depend on the characteristics of the materials to operate correctly.

The description of the developed sensor is detailed in Chapter 3. It starts by focusing on the defined optical path from coupling the laser beam to the window's interior and decoupling it to reach the photodetector. Afterward, the system's electronics are described, including the laser and corresponding driver as well as the photodiode with its amplification circuitry. It is followed by the complete system architecture and the control unit specification.

Chapter 4 covers all the performed tests and results. This chapter includes the omniphobic coating application, characterization and selection, and the contamination detection sensor tests.

Finally, in Chapter 5, the dissertation is concluded with a summary of the obtained results, and the possible future work related to the sensor is pointed out.

Chapter 2

Theoretical basis

In the following sections, the theoretical background of this dissertation is presented. The chapter starts with an overview of the relevant optics explored in this dissertation. It is followed by a description of a method for low level signal detection (lock-in amplifier) and finishes with an analysis of the glass coating properties.

2.1 Optics

Optics is a major part of this project since the working principle of the sensor is based on light propagation. Optics is the field of physics that studies the properties and behaviour of light and is frequently divided into geometrical optics and physical optics [8].

Geometrical optics is the oldest field of study in optics. This field treats light as rays that travel in straight lines. This is a simplified model that removes the necessity of using the more complex wave description of light. In most of the dissertation, this field of study provides satisfactory solutions and explanations. For this reason, this section focuses essentially on geometrical optics [9].

2.1.1 Light Propagation

Firstly, it is important to understand what light is and how it propagates through the media. Light is electromagnetic radiation, that is to say that light waves are made up of coupled oscillations of the electric and magnetic fields [10]. Electromagnetic waves are transverse waves – they oscillate orthogonally to the direction of propagation (figure 2.1).
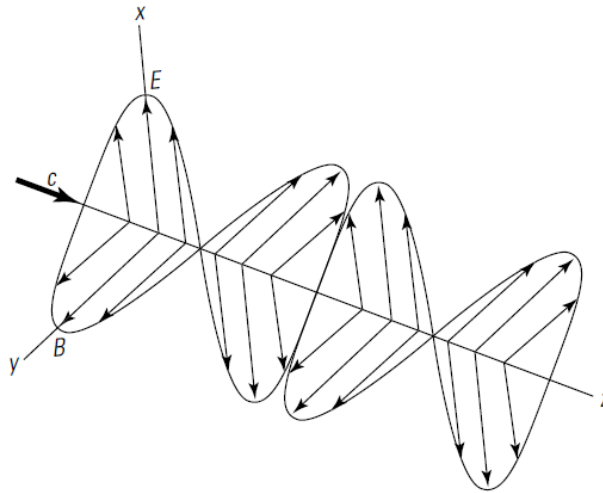
Figure 2.1: Electromagnetic wave

Although light usually refers to merely visible light, in fact, we may include the ultraviolet and infrared radiations as well – wavelengths comprised between 100nm and 1mm. These three radiations are collectively known as optical radiation, and all of them follow the laws of optics. This means that they exhibit the same behaviour, namely, diffraction, reflection and refraction. Diffraction occurs when light encounters an obstacle, such as an edge of an object or something with a hole in it, and *expands* to fill the area behind the obstacle. Reflection consists of light bouncing off a surface. It is the primary way to get information about an object (light travels from a source to an object, bounces off the object, and travels toward the receptor, delivering the information about the object). Refraction happens when the path that the light follows bends as it travels from one material into another.

2.1.2   Reflection and Refraction

Optical radiation can be reflected and refracted on the boundary between two media with distinct refractive indices. The direction that radiation takes after being reflected or refracted is described by the law of reflection and Snell's law, respectively. The first law states that the angle of reflection (θ_r) is equal to the incident angle (θ_i) (equation 2.1) [12].

$$\theta_i = \theta_r \qquad\qquad\qquad (2.1)$$
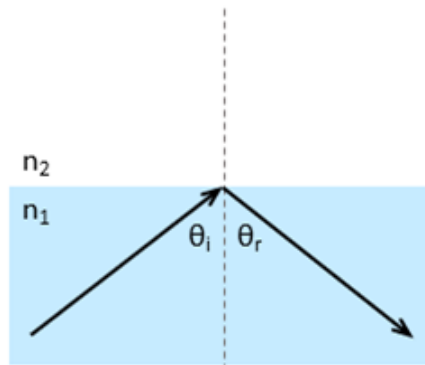
Figure 2.2: Reflection

Snell's law describes the relationship between the angles of incidence and refraction when radiation passes through the boundary between the media with different refractive indices (equation 2.2). This refractive index corresponds to the ratio between the speed of light in vacuum and the phase velocity of light in the medium. When the incident angle θ_i is fixed, the refractive indices n_1 and n_2 of those media are responsible for influencing the variation of the refracted angle θ_t [13].

$$\frac{sin\theta_t}{sin\theta_i} = \frac{v_t}{v_i} = \frac{n_i}{n_t} \tag{2.2}$$
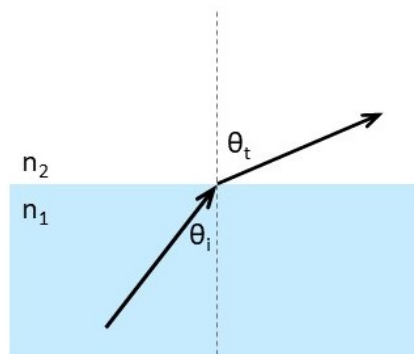
Figure 2.3: Refraction

2.1.3 Total internal reflection

When analysed the law of refraction, it is noticeable that there is a case in which the formula becomes impossible to satisfy: whenever light travels from a medium with a higher index of refraction to another with a lower one ($n_1 > n_2$), there is a limit that the angle of incidence can take. This value defines the critical angle above which the total internal reflection phenomenon occurs. Radiation with an incident

angle equal to the critical angle results in a refracted angle of 90° (figure 2.4(b)). By replacing this value on equation 2.2, the critical angle can be extracted (equation 2.3) [14].

$$\theta_c = arcsin\left(\frac{n_t}{n_i}\right)$$

(2.3)
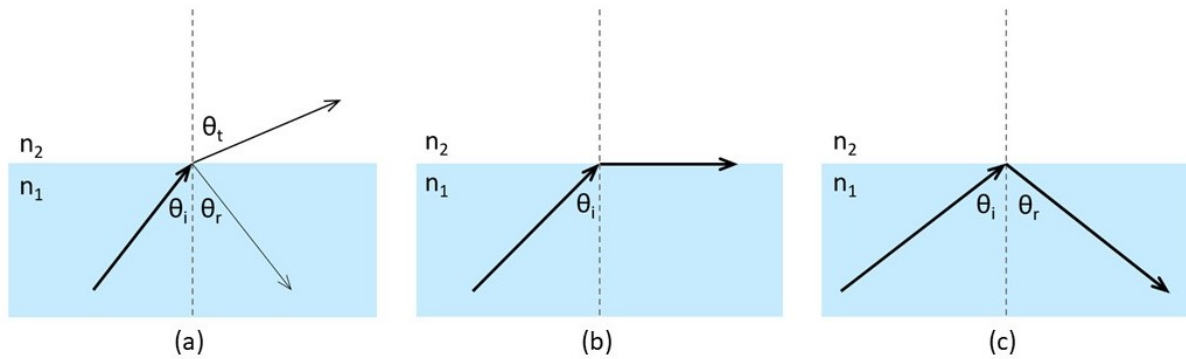
Figure 2.4: (a) Incident angle inferior to the critical angle; (b) Incident angle equal to the critical angle; (c) Incident angle superior to the critical angle

2.1.4 Ray transfer matrix

Taking into account the described principles, some optical elements can be defined by ray transfer matrices. These matrices show how the radiation direction is modified when crossing through optical elements such as lenses, mirrors, and propagation media changes and free space [15]. For ray transfer matrix calculations, the involved beam deviations must stay small for the calculations to be accurate, i.e., they require the paraxial approximation [16]. These calculations are somewhat generic and do not include losses (Beer-Lambert law), diffraction or non-linear effects.

A ray transfer matrix consists of a 2x2 matrix that describes the effect on the incident radiation. Its multiplication with the input radiation gives the resultant beam characteristics (equation 2.4). Since the radiation output as a cascade of optical elements results from matrix multiplication, it shows that optical manipulations are not commutative.

$$\begin{bmatrix} r' \\ \theta' \end{bmatrix} = \begin{bmatrix} A & B \\ C & D \end{bmatrix} \begin{bmatrix} r \\ \theta \end{bmatrix}$$

(2.4)

2.1.5   Beer-Lambert law

Until this point, radiation losses are not accounted for. However, light intensity attenuates according to the media where it propagates. All materials have a signature absorption spectrum. The absorption of radiation translates to losses.

Beer-Lambert law refers to the attenuation of light propagation to the material's properties through which light is travelling. According to this law, the intensity of injected light in a material reduces with the increase of the media's absorptivity and the optical path length (equation 2.5) [17]. In other words, radiation transmittance reduces with the increase of absorbance of the media and the path length that the radiation has to travel through.

$$I_x = I_0 e^{-ax} \tag{2.5}$$

$I_x =$ Intensity of light after passing through the material

$I_0 =$ Intensity of light before passing through the material

$a \ \ =$ Absorptivity of the material

$x \ \ =$ Optical path length

2.1.6   Polarization

So far, light's behaviour was analysed when encountering a boundary of two different media: reflection and refraction. The laws of reflection and refraction allow to figure out the directions that light will follow. However, they do not give any information regarding how much of the incident light follow each path.

Fresnel developed a way to quantify how much light is reflected and transmitted (refracted), in other words, calculate the reflectance and transmittance. There are two sets of formulas, one for each polarization: *s* and *p* (figure 2.5. As previously described, light is composed of electric and magnetic waves perpendicular to each other that oscillate perpendicular to the direction of propagation. In order to identify the polarization, the electric field orientation is compared to a plane where the incident, reflected and refracted rays are placed, also known as the plane of incidence.

If the incident light has its electric field oriented perpendicular to the plane of incidence, the polarization of the light is referred to as *s* polarization (from the German *senkrecht*). In the opposite case, if the incident light has its electric field oriented parallel to the plane, the polarization of the light is referred to as *p* polarization (from the German *parallel*) [18].
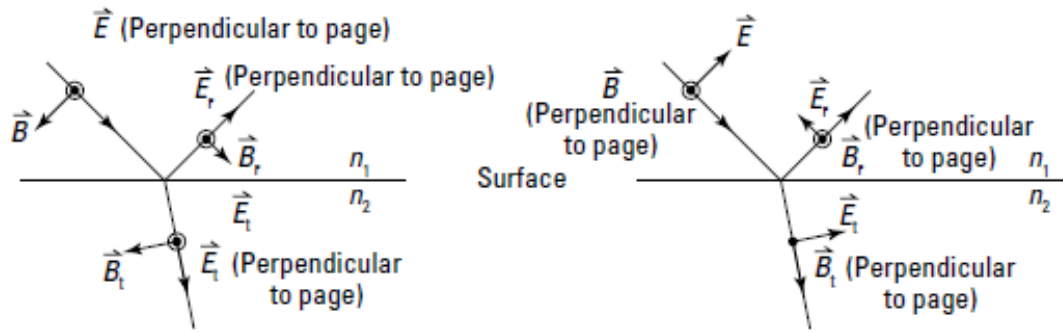
Figure 2.5: On the left is represented *s* polarization and on the right is *p* polarization

The polarizations represent two extreme cases, thus any orientation of fields in the incident light can be made of these two polarizations, just like a two-dimensional vector can be decomposed into two orthogonal components.

The Fresnel equations are four equations used to determine how much light appears in the reflected and transmitted waves as a fraction of the incident light. They are derived from the boundary conditions for electric and magnetic fields as they encounter a surface.

$$r_s = \frac{n_i cos\theta_i - n_t cos\theta_t}{n_i cos\theta_i + n_t cos\theta_t} \quad (2.6) \qquad t_s = \frac{2n_i cos\theta_i}{n_i cos\theta_i + n_t cos\theta_t} \quad (2.7)$$

$$r_p = \frac{n_t cos\theta_i - n_i cos\theta_t}{n_i cos\theta_t + n_t cos\theta_i} \quad (2.8) \qquad t_p = \frac{2n_i cos\theta_t}{n_i cos\theta_i + n_t cos\theta_i} \quad (2.9)$$

The equations 2.6 to 2.9 give the respective reflection and transmission coefficients, which can be used to determine reflectance and transmittance by simply squaring the obtained coefficients(equations 2.10 to 2.13).

$$\mathcal{R}_s = r_s^2 \quad (2.10) \qquad \mathcal{T}_s = t_s^2 \quad (2.11)$$

$$\mathcal{R}_p = r_p^2 \quad (2.12) \qquad \mathcal{T}_p = t_p^2 \quad (2.13)$$

2.1.7   Impedance matching

The Fresnel equations are based on the impedance of the media. Since almost all optical materials are non-magnetic ($\mu_r \approx 1$), the wave impedance depends only on the refractive index (equation 2.14). For that reason, equations 2.6 to 2.9 contain the refractive index of the media instead of the respective impedances.

$$Z = \frac{Z_0}{n} \qquad (2.14)$$

Similarly to electronics, optical impedance matching can be achieved in order to reduce and minimize reflection. The addition of a coating on an interface can reduce the overall reflectance in case its refractive index is between the refractive indices of the materials that it is separating. When the reflectance value is equal in both interfaces, the coating has the optimal refractive index. The optimal coating refractive index reduces the overall reflectance to a minimum and can be obtained with equation 2.15 [19].

$$n_c = \sqrt{n_1 n_2} \qquad (2.15)$$

Furthermore, reflection can be reduced by exploring the interference phenomenon. If the coating has a thickness of one quarter of the wavelength of the emitted radiation, there will be destructive interference of the reflections. The reflection from the second interface travels half of its wavelength more than the reflection from the first interface; the waves have a phase difference of 180°, leading to cancel each other.

2.1.8   Finite-Difference Time-Domain Method

The optical principles presented above are the required aspects to consider for developing this dissertation's sensor.

To simulate some of the principles, the Finite-Difference Time-Domain (FDTD) method is a numerical analysis technique that allows modelling computational electrodynamics. This method is based on a spatial and temporal discretization of Maxwell's equations and enables the creation of calculation and animation of propagating waves through various materials. Starting from the derivative form of Maxwell's equations, the electromagnetic wave equations can be deduced and later discretized. Since the goal is to make possible to compute the wave equations, some approximations are necessary to be done. The following equations show the steps taken to reach to computerizable electromagnetic waves.

In the absence of free charges and currents, Maxwell equations are:

$$\nabla \cdot E = 0 \tag{2.16}$$

$$\nabla \cdot B = 0 \tag{2.17}$$

$$\nabla \times E = -\frac{\partial B}{\partial t} \tag{2.18}$$

$$\nabla \times B = \mu_0 \epsilon_0 \frac{\partial E}{\partial t} \tag{2.19}$$

$E =$ Electric Field

$B =$ Magnetic Field

The first step consists of using Maxwell's equations (equations 2.16 to 2.19) to extract the wave equations (equations 2.21 and 2.22).

$$c = \frac{1}{\sqrt{\epsilon_0 \mu_0}} \iff \frac{1}{c^2} = \epsilon_0 \mu_0 \tag{2.20}$$

$$\nabla^2 E = \frac{1}{c^2}\frac{\partial^2 E}{\partial t^2} \tag{2.21}$$

$$\nabla^2 B = \frac{1}{c^2}\frac{\partial^2 B}{\partial t^2} \tag{2.22}$$

From now on, the steps shown are only for the electric field, but the same process can be used for the magnetic field.

Considering only one dimension, the Laplacian operator corresponds to the spatial derivative in a single axis (equation 2.23).

$$\frac{\partial^2 E}{\partial x^2} = \frac{1}{c^2}\frac{\partial^2 E}{\partial t^2} \tag{2.23}$$

The second order spatial derivatives can be replaced by the respective definition of derivative as shown on equation 2.24.

$$\lim_{x \to 0} \frac{E(x + \Delta x) - 2E(x) + E(x - \Delta x)}{\Delta x^2} = \lim_{t \to 0} \frac{1}{c^2} \frac{E(t + \Delta t) - 2E(t) + E(t - \Delta t)}{\Delta t^2} \quad (2.24)$$

Applying the finite-difference technique, it can be said that equation 2.24 is approximately what is shown on equation 2.25.

$$\frac{E(x + \Delta x) - 2E(x) + E(x - \Delta x)}{\Delta x^2} \approx \frac{1}{c^2} \frac{E(t + \Delta t) - 2E(t) + E(t - \Delta t)}{\Delta t^2} \quad (2.25)$$

The goal of this deduction is to obtain a computational version of electromagnetic radiation. Thus, FDTD implementation is assumed that the approximation in equation 2.25 corresponds to an equality (equation 2.26).

$$\frac{E(x + \Delta x) - 2E(x) + E(x - \Delta x)}{\Delta x^2} = \frac{1}{c^2} \frac{E(t + \Delta t) - 2E(t) + E(t - \Delta t)}{\Delta t^2} \quad (2.26)$$

Following the same steps but for the magnetic field, the respective solution is shown in equation 2.27.

$$\frac{B(x + \Delta x) - 2B(x) + B(x - \Delta x)}{\Delta x^2} = \frac{1}{c^2} \frac{B(t + \Delta t) - 2B(t) + B(t - \Delta t)}{\Delta t^2} \quad (2.27)$$

The FDTD method was successfully implemented on Matlab from scratch without using any electromagnetism library. However, due to the dimension of the desired simulation, the computational load was very high, and the simulation of the pretended optical system was not developed fully.

2.2 Lock-in Amplifier

Usually, measurements in electronics can be performed with scientific equipment such as an oscilloscope or a multimeter. This applies whenever the signal to noise ratio is significant and sufficient. When the noise has similar or superior proportion than the signal, this task becomes practically impossible with those equipments. In this case, a lock-in amplifier is necessary.

Lock-in amplifiers allow to measure the amplitude and the phase of a signal relative to a defined reference signal, even if the signal is entirely buried in noise (figure 2.6). In other words, lock-in amplifiers allow to extract the wanted signal from a larger obtained signal (noise included).
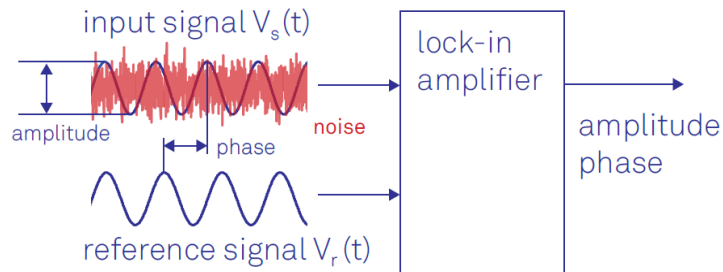

Figure 2.6: Overview of a lock-in amplifier [23]

The lock-in amplifier HF2LI from Zurich Instruments was used in this dissertation (figure 2.7). It is a digital lock-in amplifier covering the frequency range between DC and 50MHz.

In this dissertation, the lock-in amplifier was used to measure light scattering out of the protective window. Scattered radiation corresponds to a very low percentage of the injected beam. By feeding the reference signal to the laser, scattering can be detected in the signal captured by the photodiode.

Figure 2.7: Zurich Instruments HF2LI [24]

2.3 Coatings

One of the dissertation's goals is to maintain the protective window as clean as possible without the necessity of any intervention. Thus, contamination such as water, dirt and hydrocarbons has to be minimized.

In order to do so, the window surface can be manipulated so that it becomes repellent to contamination. The surface manipulation can be made via the application of an omniphobic coating.

Surface repellency is characterized by the wettability and roll-off ease of a liquid droplet. Surface wettability indicates the wetting state of a surface, which defines if a surface becomes wet or repels a liquid. This surface property is primarily characterized by the contact angle, defined by the angle formed between a liquid drop and the surface. A contact angle inferior to 90° indicates that the surface is liquiphilic. Contact angles above 90° define a surface as liquiphobic. In case that angle is superior to 150°, the surface is considered superliquiphobic (figure 2.8).
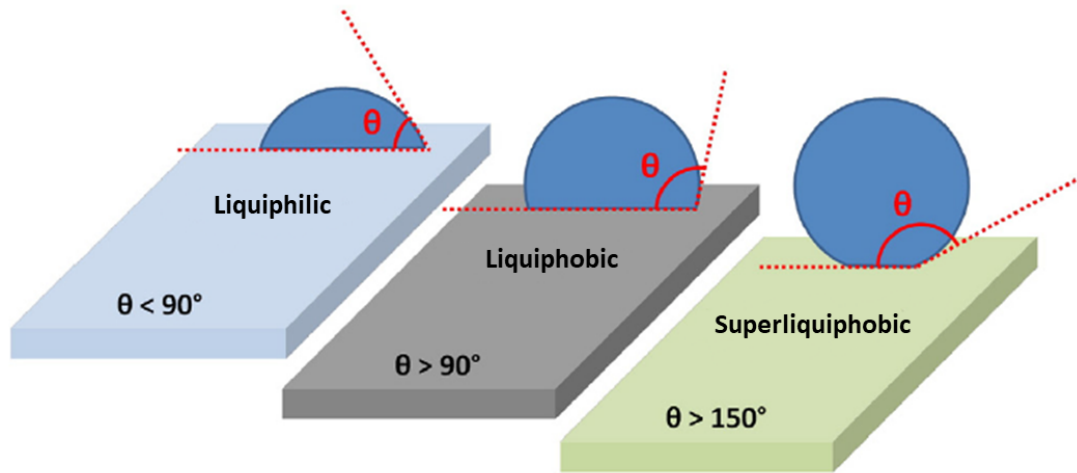
Figure 2.8: Surface classification [25]

Besides that, the contact angle hysteresis is an important parameter. When a surface has some inclination, the droplet movement means that the contact angle at the front is greater than at the back. Contact angle hysteresis corresponds to the difference between these angles and indicates how sticky a droplet is to a surface.

Figure 2.9: Cassie-Baxter state

The surface roughness can decrease the contact angle hysteresis, according to the Cassie-Baxter model (figure 2.9). The model defines a rough surface where the droplet sits on top of solid structures

and traps air between them and the liquid. The droplet rests on top of air and solid composite, which reduces the attraction of the surface. Consequently, the contact angle hysteresis is lower and allows a more effortless roll-off ability.

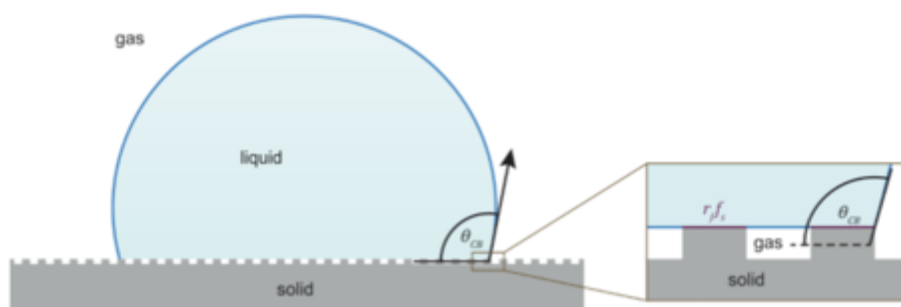An omniphobic surface displays contact angles greater than 150° and low contact angle hysteresis with both polar (e.g. water) and nonpolar (e.g. hydrocarbons) liquids possessing a wide range of surface tensions [26]. Creating a surface able to repel nonpolar liquids is very challenging. These liquids present a low surface tension (3 times inferior than water), which requires a complex surface.

2.4 Technologies

In this section, technologies with somewhat similar working principles to the contamination detection sensor are presented. Both fibre optic communication and the automotive rain sensor explore the concept of total internal reflection. The first one, to transmit information without losses, and the second is designed to stop reflecting when there is water.

2.4.1 Fibre optic communication

Before the appearance of optical cables, information was carried by electrical signals in wires made of copper. This was slow and inefficient due to the metal wires speed limitation and the power losses by heat. Optical fibres replace the metal wire with fibreglass in its core with a higher refractive index than the cladding. The difference of refractive indices between these materials allow to inject beams with an angle of incidence inferior to the critical angle, i.e. it allows total internal reflection of the radiation. Total internal reflection allows the information to travel as pulsed radiation [27].
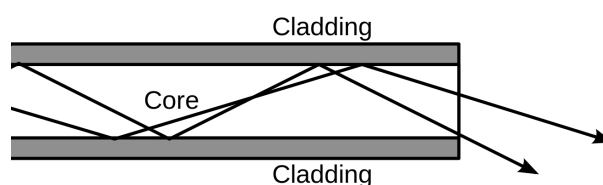

Figure 2.10: Optical fibre cable

Optical cables allow huge data rates with almost no losses (some minor losses due to scattering). Its structure presents a disadvantage: optical cables cannot be bent. Bending them beyond a certain

angle would modify the angle of incidence on the second medium, and, consequently, the radiation would escape the interior of the cable.

2.4.2 Automotive rain sensor
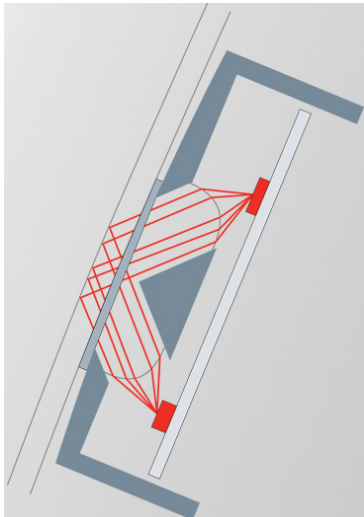
Figure 2.11: Dry windshield, total reflection [28]
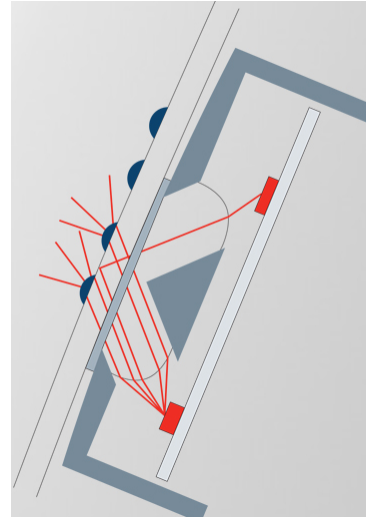
Figure 2.12: Wet windshield, light beam broken [28]

The automotive rain sensor is an example of a device that uses the concept of total internal reflection to detect if there is water in the windshield. The sensor consists of a light beam guided via a prism to the windshield, where the beam is reflected by the outer windshield surface and forwarded to the photodiode (figure 2.11). The incident light beam has an angle of incidence larger than the critical angle, so there is total internal reflection. When there are raindrops on the windshield, the refractive index of the exterior increases, which means that the critical angle decreases. Consequently, the incident beam no longer has an angle superior to the critical angle; thus, the light is not totally reflected. With the increase of water quantity on the windshield, the intensity of light that reaches the photodiode decreases (figure 2.12).

Chapter 3

Sensor

The contamination detection sensor explores the concept of internal reflection to detect the contaminants on the surface of the protective window. Similar to fibre optics, a light beam is guided through the window's section from one end to the other. In fibre optics, the goal is to get all the injected radiation at the end of the cable; hence the beam's angle being reflected internally is desired to be consistently superior to the critical angle. This condition determines that there are no losses to the exterior and the totality of injected radiation reaches the other end.
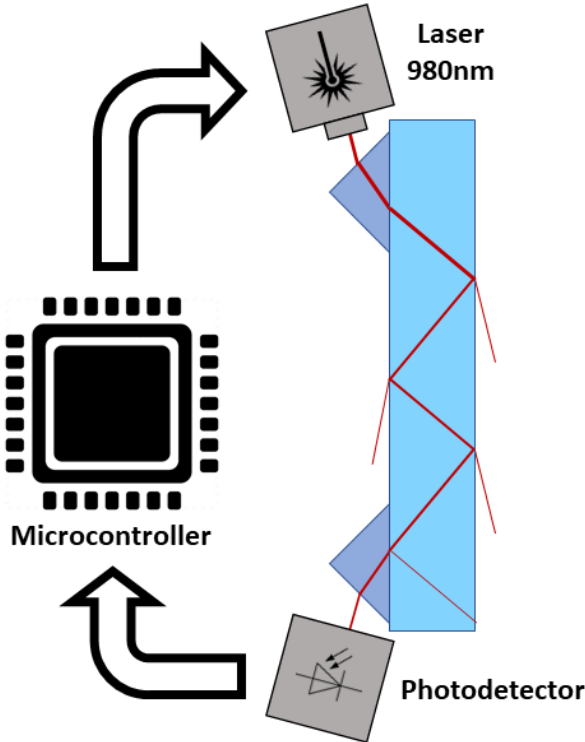

Figure 3.1: System overview

Unlike fibre optics, in the contamination detection system, the angle of incidence is configured as just

below the critical angle. This configuration means that there is a tiny portion of radiation escaping the window's interior. The reason to configure it this way is the ability to detect a wide range of materials with different spectroscopy properties. In case the window is contaminated with a material that increases the "escape" of light to the exterior, such as water, the intensity of radiation reaching the photodetector decreases (figure 3.2(b)). On the other hand, if the contamination is a material that presents high reflectivity, e.g. mica found on dirt and mud, the radiation's intensity reaching the photodetector increases (figure 3.2(c)).
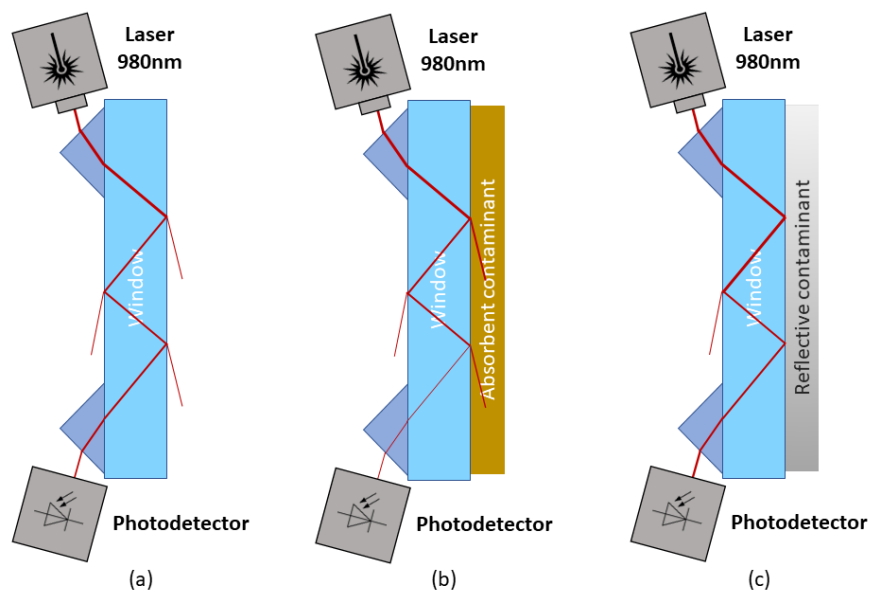
Figure 3.2: Window contamination scenarios: (a) without contamination, (b) contaminated with radiation absorbent material, and (c) contaminated with reflective material.

In order to achieve the desired light beam angle, two prisms were used to guide the beam to the window's interior and decouple it to reach the photodetector. The photodetector is the element responsible for quantifying the intensity of light that travels through the window. On the other end of the system, a laser diode injects the light beam at the desired angle of incidence. A microcontroller controls these elements: activates and deactivates the laser at the right time and reads the radiation intensity captured by the photodetector. Besides that, it is responsible for communicating with the Road Condition Sensor.

3.1 System Architecture

The architecture of the contamination detection sensor is depicted in figure 3.3. It represents the elements and resources of the sensor as well as the connections with the RCS. The system has 4 main

elements: the photodetector, the laser, the optical path between them and the microcontroller.
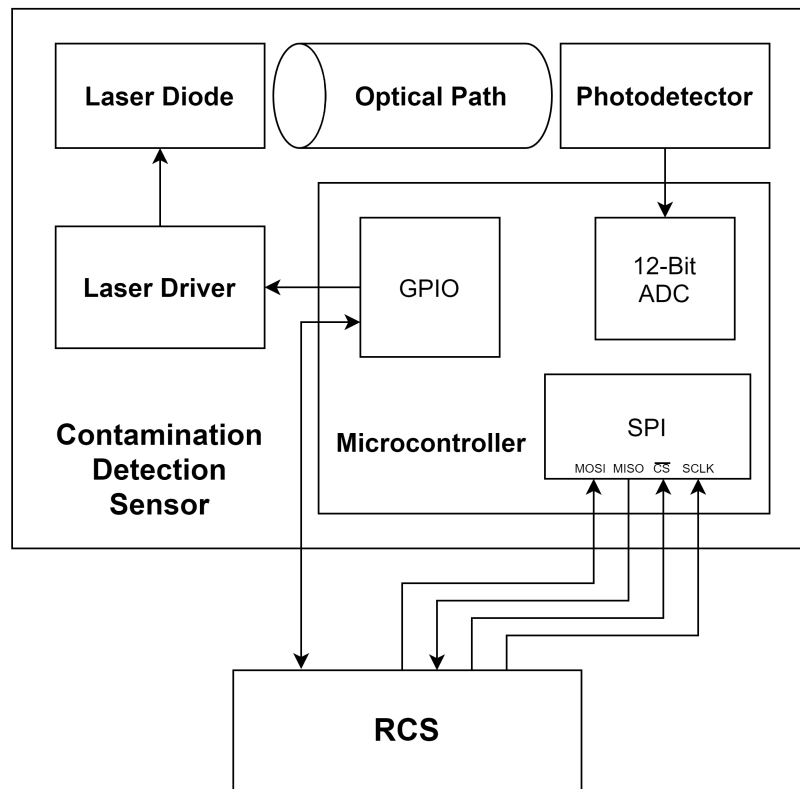
Figure 3.3: System architecture

In the following sections, each element of the system is described in detail. Firstly, the optical setup is determined and described. This section includes a discussion of the angle of incidence and the importance of using prisms and a coupling gel. After that, the hardware of the system is described. The laser and photodetector components selection and the respective circuitry is described in this section. The last section contains a description of the interaction between the laser, photodetector, microcontroller and the Road Condition Sensor.

3.2 Optical System

In this section, every aspect of the optical path between the laser and photodiode is described. It starts by analyzing the conditions dictated by the characteristics of the materials and it is followed by the decisions made to achieve the desired optical path.

Figure 3.4: Optical system in the system overview

As a means to assemble the prototype, the coupling and decoupling angles have to be determined. They can be calculated taking into consideration Snell's law and Fres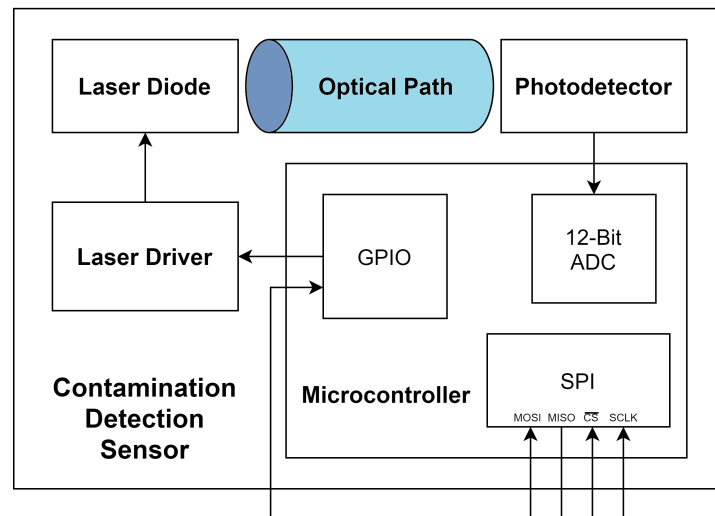nel equations. In these formulas, the refractive indices of the window's material and the medium are necessary to be known. The window is made of polycarbonate, and its refractive index is 1.58, and the medium is air, so the refractive index is 1.

$$n_{window} = 1.58$$

Firstly, the interface's critical angle between the window and the air can be obtained with these refractive index values using equation 2.3.

$$\theta_c = 39.265°$$

With the help of coupling prisms, the light beam can be guided through the window. Coupling prisms allow to optically couple and decouple the radiation, which makes it possible for light to travel from the laser diode, through the window's interior and to reach the receptor. The prisms are made of Gadolinium Gallium Garnet and have a refractive index of 1.946 at 980nm.

$$n_{prism} = 1.946$$

The presence of air between the prisms and the window considerably reduces the intensity of light guided through the window and reaches the receptor (figure 3.5). Since the surfaces are not perfectly flat and smooth, the existence of air molecules on this interface is inevitable. For that reason, an index

matching gel is used to reduce the signal attenuation on the interface between media (figure 3.6). This gel has a refractive index of 1.4462 at 980nm.

$$n_{gel} = 1.4462$$
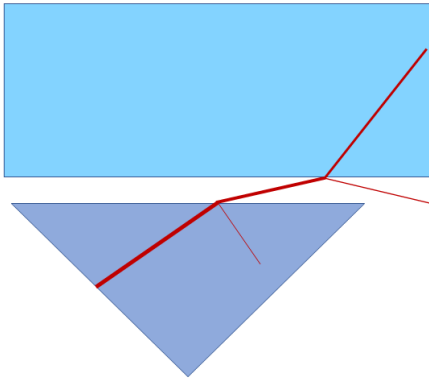
Figure 3.5: Prism to window interface without Gel
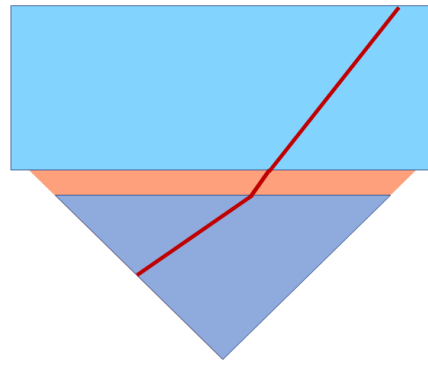
Figure 3.6: Prism to window interface with Gel

Prism → Air

$$\mathcal{T}_s = 40.4\%$$

$$\mathcal{T}_p = 88.1\%$$

Air → Window

$$\mathcal{T}_s = 50.6\%$$

$$\mathcal{T}_p = 84.5\%$$

Prism → Window

$$\mathcal{T}_s = 20.4\%$$

$$\mathcal{T}_p = 74.4\%$$

Prism → Gel

$$\mathcal{T}_s = 95.0\%$$

$$\mathcal{T}_p = 99.5\%$$

Gel → Window

$$\mathcal{T}_s = 99.4\%$$

$$\mathcal{T}_p = 99.98\%$$

Prism → Window

$$\mathcal{T}_s = 94.4\%$$

$$\mathcal{T}_p = 99.5\%$$

The transmittance values above correspond to the intensity of light transmitted in both cases (with and without index matching gel). The usage of an index matching gel presents a considerable advantage since the transmittance is substantially increased. Consequently, most of the energy from the laser can be coupled to the window. With the help of the gel, the insertion losses are practically negligible in both polarizations.

3.2.1   Coupling

Inside the window, the light beam reflects multiple times on the interface window-air before reaching the receptor. Each time it hits this interface, a substantial part of the radiation must be kept inside the window whilst the remaining is transmitted to the outside. This means that the angle of incidence on this surface shall be slightly lower than the critical angle. As mentioned earlier, this configuration allows for the identification of a wide variety of contaminants. Since the elements available to build the setup do not allow a high resolution, the structure aims to obtain a value of α ranging between 38° and 39°. The closer the angle is to 39°, the better since more radiation is kept inside the window. The θ angle is selected in function of β, which in turn is selected accordingly α. The following values represent the resultant angles of the extremes of the determined range for α (figure 3.7).
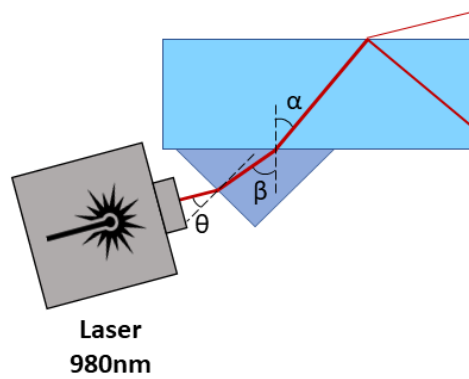
Laser
980nm

Figure 3.7: Coupling Angle

$$\alpha_1 = 38° \qquad\qquad \alpha_2 = 39°$$

$$\beta_1 = 29.99° \qquad\qquad \beta_2 = 30.73°$$

$$\theta_1 = 30.26° \qquad\qquad \theta_2 = 28.67°$$

$$\textbf{Window} \rightarrow \textbf{Air} \qquad\qquad \textbf{Window} \rightarrow \textbf{Air}$$

$$\mathcal{R}_s = 47.1\% \qquad\qquad \mathcal{R}_s = 70.7\%$$

$$\mathcal{R}_p = 13.3\% \qquad\qquad \mathcal{R}_p = 41.5\%$$

$$28.67° < \theta < 30.26°$$

The laser diode shall be positioned in order to create an angle of incidence between 28.67° and 30.26°. The resolution of the mechanical setup does not allow to position the laser beam with much accuracy, so the select angle has to be an integer. That is to say, the selected angle should be 29° or 30°. With a θ angle of 29°, α is closer to 39°, which is considered to be ideal. However, the inaccuracy of the setup could mean that the expected θ angle is, in fact, lower, which can result in an α angle value higher than the critical angle. Considering this, θ is aimed to be 30°, reducing the risk of having total internal reflection and still having a significant amount of internally reflected radiation inside the window. Assuming θ is 30° results in:

$$\alpha = 38.16°$$

Window $\rightarrow$ Air

$$\mathcal{R}_s = 49.4\%$$

$$\mathcal{R}_p = 15.5\%$$

3.2.2 Decoupling

On the other side of the system, there is a photodetector receiving radiation originated from the laser diode. In order for the receptor to be able of quantifying the intensity of light that is crossing the window, the radiation must be decoupled out the window's interior. To do so, it is necessary to implement the same setup as the one on the side of the emitter. Basically, the setup is equal to the coupling implementation, and the values of the angles in figure 3.8 are the same as previously determined. This means that the photodetector is positioned with the same inclination as the laser diode.
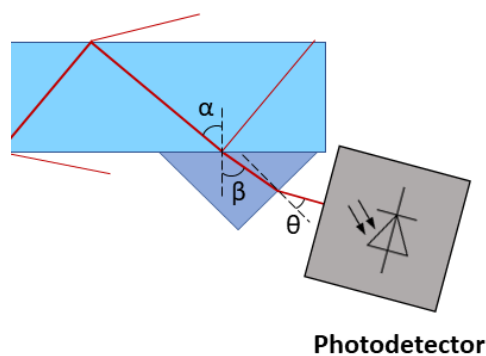

Photodetector

Figure 3.8: Decoupling Angle

3.3   Hardware

In this section, the hardware of the system is described in detail. Firstly, the laser characteristics are exposed and as well as the circuitry used to drive it. Besides the electronics involved, the correction of the laser beam with a lens is also explained.

Along with that, the hardware also includes the photodetector circuitry. It starts by providing a brief explanation of the working principle of a photodiode that highlights some fundamental considerations that help decide the mode of operation of the photodiode. Considering these aspects, the amplification circuit implementation is described thoroughly.

3.3.1   Laser

The laser diode emits a light beam through the defined optical path. This laser is accompanied by a driver that controls and stabilizes the laser output. The involved circuitry for the laser implementation is described below.
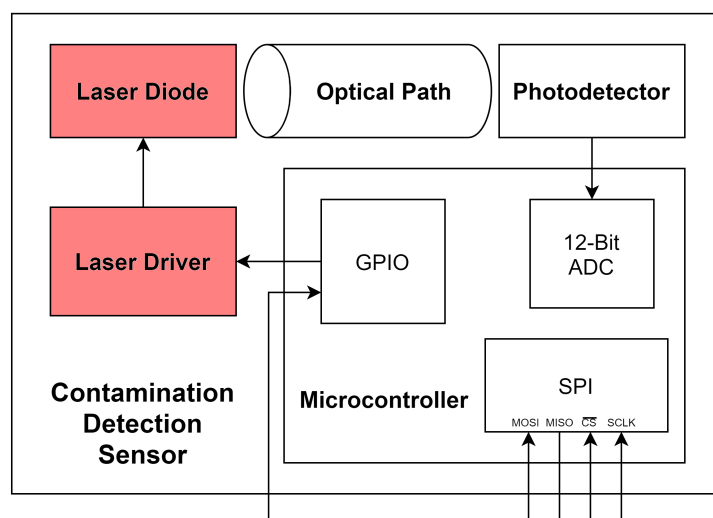
Figure 3.9: Laser in the system overview

The laser selection is based on exploring scale economy, so a laser with one of the wavelengths used by the RCS (980nm, 1310nm, 1410nm or 1550nm) must be selected. The developed sensor requires the laser to be contained in a small package which allows mounting it on a PCB in a fixed position. Within these options, price and efficiency are other relevant factors to be considered. Since all lasers present similar efficiency, price became the decisive factor. The selected laser is much cheaper than the alternatives and meets every other requirement.

The selected laser diode is the L980P010 from Thorlabs [30], a compact and low power light source encapsulated in a TO-18 package (figure 3.10). This component has maximum output power of 10mW and a centre wavelength of 980nm.
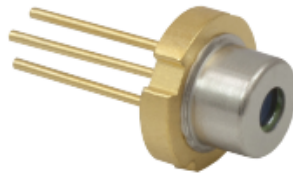

Figure 3.10: Laser diode L980P010.

Lasers are extremely sensitive and can be easily damaged by the power supply if it is not stable enough. For this reason, a driver capable of dealing with the sensitivity of lasers is necessary to power it. The selected driver is the iC-NZN from iC-Haus, a component specifically designed to maintain a stable current through laser diodes. iC-NZN is a laser diode pulse driver which allows continuous wave operation of laser diodes and spike-free switching with defined current pulses up to 155 MHz.
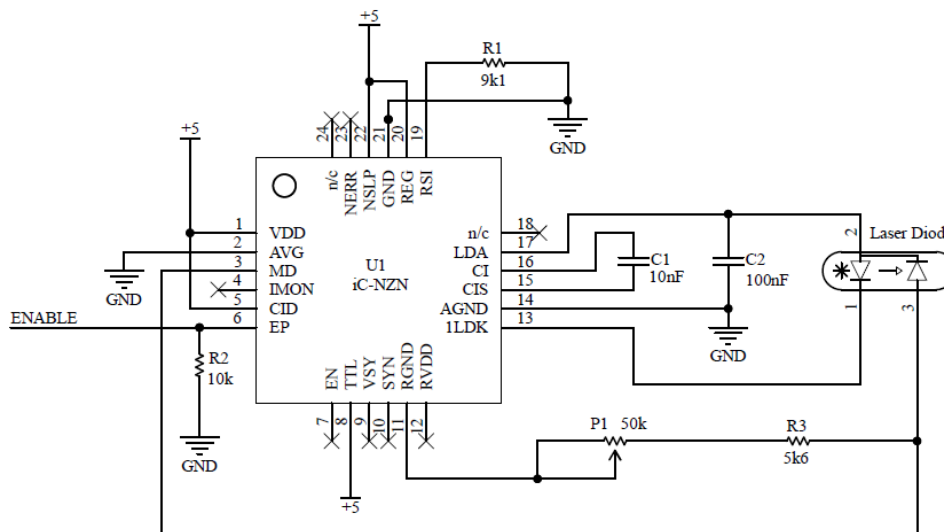
Figure 3.11: Circuit schematic of laser driver

The schematic of the laser driver circuit that was implemented is depicted in figure 3.11. Since the selected laser diode is an N-type one, the circuit is configured accordingly. The desired optical output power of the laser diode is set up by means of an external resistor (R3 and P1) connected to the monitor diode of the laser. R3 and P1 have to be calculated considering the minimum and maximum values of monitor current accepted by the laser diode. This pair of components must be chosen so that the monitor

current generated by the desired output power creates a voltage drop of 500mV across them. The control circuit monitors the laser current in pin ILDK and limits this current when reaching the threshold defined by RSI (where R1 is connected). Resistor R1 is calculated according to the maximum value of current that the photodiode can receive.

Figure 3.12: Lens

The laser diode output is highly divergent and needs to be collimated. So, a collimating lens is required. Spherical aberration is a phenomenon that is seen in spherical lenses and consists of an optical effect that causes incident light rays to focus at different points when forming an image (figure 3.13) [31]. In order to minimize this aberration, an aspheric lens[1] can be used [32].
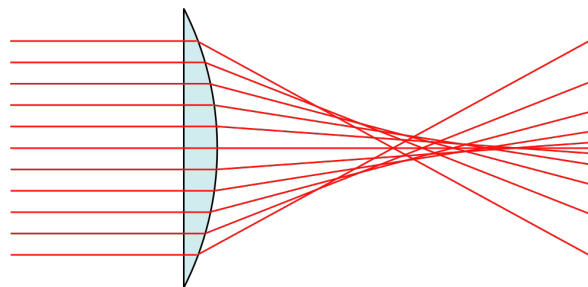

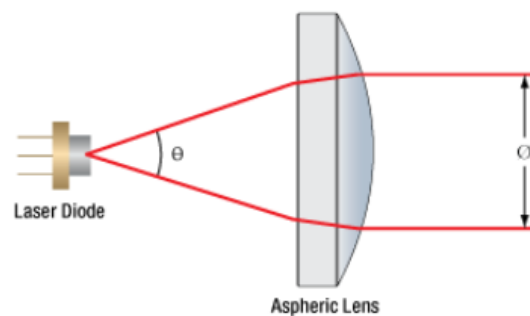Figure 3.13: Spherical aberration

Figure 3.14: Laser divergence and desired output diameter

[1]Lens with a complex surface that is not a portion of a sphere.

For selecting the lens, it is essential to know the divergence angles of the laser diode being used and the desired output diameter (figure 3.14). The specifications for the L980P010 indicates that the typical parallel and perpendicular beam divergence is 13° and 30°, respectively. With the purpose of collecting as much light as possible during the collimation process, it is considered the larger of the two divergences in all calculations. The desired beam diameter is to be inferior to half of the window thickness (3mm). If the output is assumed to be precisely half (1.5mm), the effective focal length of the lens must be:

$$f = \frac{1.5mm}{tan15°} = 5.6mm$$

Since the output diameter is desired to be inferior to 1.5mm, the effective focal length must be inferior to 5.6mm.

The selected lens is C230TMD-B from Thorlabs (figure 3.12). This lens is an aspheric lens with an effective focal length of 4.51mm, resulting in a beam diameter of 1.21mm. An aspect to take into account is the numerical aperture[2] of the lens and the laser [33]. The numerical aperture of the lens must be greater than that of the laser. The numerical aperture of the laser can be calculated by multiplying the refractive index of the medium with the sine of the divergence's angle.

$$NA_{laser} = n_{air}sin15° = 0.26$$

The numerical aperture of the lens is 0.55, so its value is much greater than the numerical aperture of the laser.

The wavelength of the laser's output is a relevant parameter when selecting the lens due to the type of Anti Reflective coating that it has to contain. Another decisive factor was the price of this lens, and this lens is the cheapest compared with others with similar characteristics.
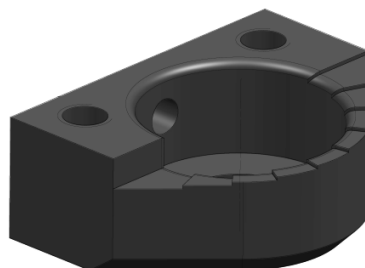
Figure 3.15: Lens Mount (Produced by Bosch)

---

[2]NA: dimensionless number that characterizes the range of angles over which the system can accept or emit light.

In order to attach the lens, a lens mount produced by Bosch was used (figure 3.15). This lens mount allows screwing the lens on the desired distance of the laser diode. The mount allows adjustments in the position of the lens and obtain the intended collimation.

Figure 3.16: PCB layout of laser circuitry

The PCB layout of the laser driver is shown in figure 3.16. The laser (figure 3.10), lens (figure 3.12) and respective mount (figure 3.15) are placed on the underside of the board.

3.3.2 Photodetector

Figure 3.17: Photodetector in the system overview

In the other end of the optical path, the photodetector captures the beam originated from the laser.

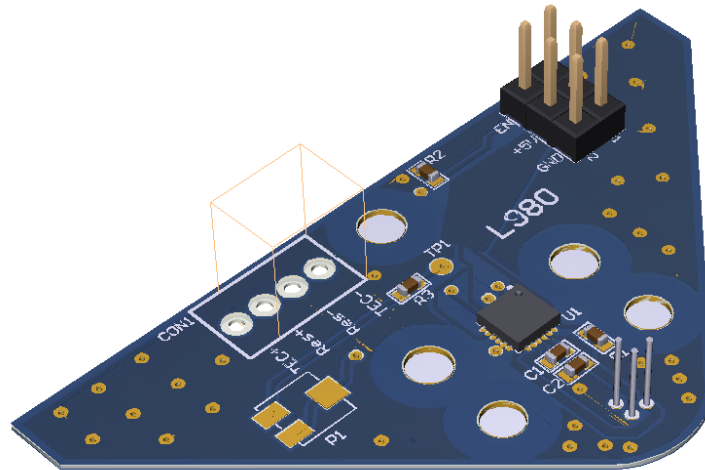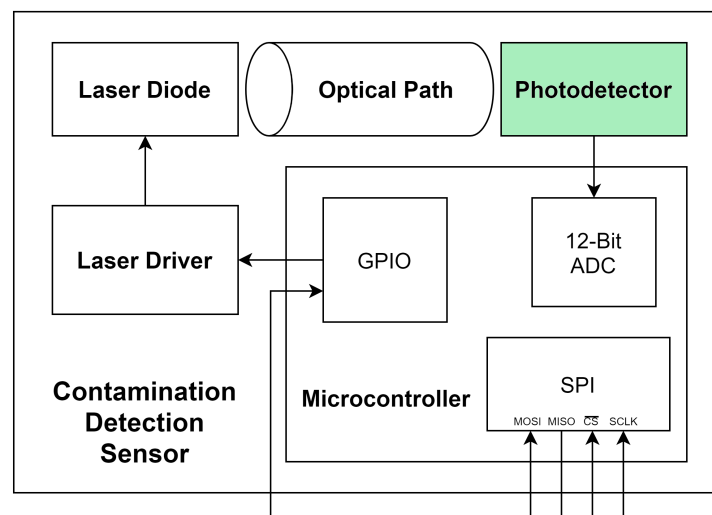The photodetector consists of a photodiode and an amplification circuit. The photodiode is responsible for converting light intensity into electrical current. This component generates a flow of current in an external circuit, proportional to the incident power of the radiation. The selected component is the G12180-003A from Hamamatsu (figure 3.18); an InGaAs PIN photodiode with a photosensible area of 0.3mm and capable of detecting radiation with wavelengths between 900nm and 1700nm. The latter is the main characteristic when looking for an adequate photodiode for the system, where a laser beam of 980nm is injected. For this wavelength, the photodiode has a photosensitivity of approximately 0.5A/W.

Figure 3.18: Hamamatsu G12180-003A [34]

As aforementioned, the photodiode generates a current proportional to the light that strikes its active area. Photodiodes are basically the same as the standard diode but with their sensitive area exposed to light in an optimised manner. The photodiode follows the principle of internal photoelectric effect. When it is illuminated by radiation with greater photon energy than the band gap, the valence electrons are excited to the conduction band [35]. Photon energy is inversely proportional to the wavelength, while light intensity affects the rate of photoelectrons; thus it affects the generated current.

Photodiodes are manufactured from various materials, each presenting different properties for wavelength range and sensitivity, for instance. Besides that, there are different types of photodiodes junctions such as P-N and PIN. The most basic photodiode is the one with P-N junction. As its name suggests, this junction consists of the union of two types of doped semiconductors: n-type and p-type. The n-type side is doped with an impurity that increases the number of electrons present on the pure semiconductor. On the other hand, p-type substrate is the result of doping with a substance that creates holes. These holes correspond to lack of an electrons within the substrate. This lack and excess of electrons on each side allow electrical current to pass through the junction only in one direction: from the positive to the negative side.

Photodiodes can operate in two distinct modes: photovoltaic or photoconductive. In photovoltaic mode, the photodiode is unbiased, that is, without any applied voltage. In this case, the depletion region

width is the smallest since photodiodes are not operated forward biased as diodes. In photoconductive mode, the photodiode is reverse biased: the p-side is connected to a voltage inferior to the one connected to the n-side.

The depletion region is an area of considerable resistance and, for that reason, can be compared to a dielectric. Therefore a semiconductor with a p-n junction can be assumed to have a behaviour similar to a capacitor. In a capacitor, the capacitance is defined by the distance between plates, contact area and type of dielectric. In a diode, the same applies, although the distance between plates is, in fact, the width of the depletion region. So the diode's capacitance can be manipulated by changing the width of the depletion region. The depletion region changes accordingly to the applied bias voltage. Reverse biasing the diode results in an increase in the width of the depletion region. Consequently, the capacitance of the diode decreases with the increase of reverse bias voltage. Decreasing the capacitance results in a decrease in charging time, so the response speed is higher. At the same time, resistance increases with the width of the depletion region since the energy necessary for an electron to flow from the n-side to p-side is more significant (figure 3.19). Reverse biasing a p-n junction is a technique explored by varicaps for capacitance manipulation.
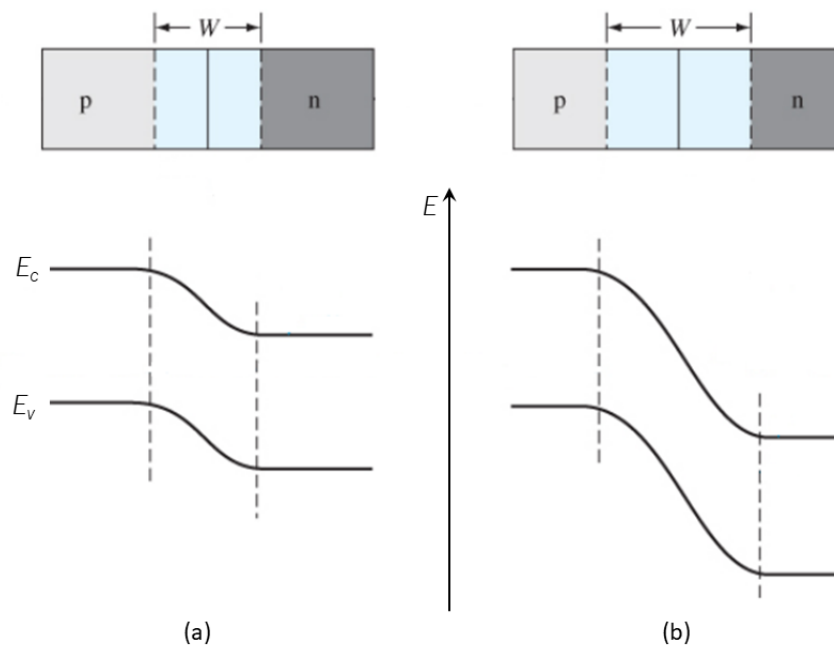

Figure 3.19: P-N junction band diagram for zero bias (a) and reverse bias (b).

However, increasing the reverse bias voltage increases the dark current as well. Dark current, also known as leakage current, appears when applied a reverse bias voltage to a photodiode (figure 3.20).
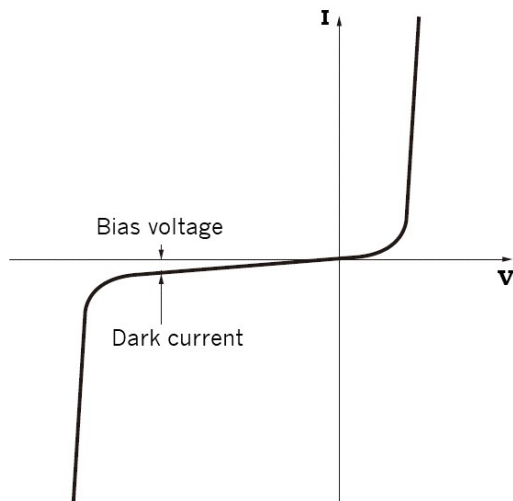
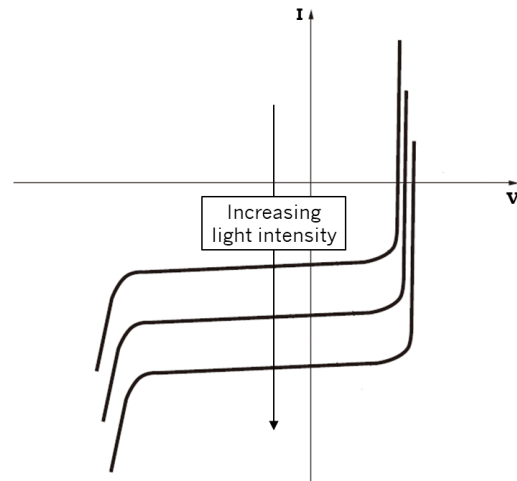Figure 3.20: Diode current-voltage characteristic curve

Figure 3.21: Photodiode current-voltage curves when sensing light

When light strikes the photodiode, its characteristic curve shifts vertically accordingly to the generated current, so dark current corresponds to electrical noise that is always present during the operation of the photodiode (figure 3.21).

The PIN photodiode is similar to the P-N but with an intrinsic semiconductor region between the n-type and p-type doped regions. The intrinsic semiconductor is an undoped region where its number of holes and excited electrons are equal. The addition of the intrinsic region increases the depletion region width, which means that this type of photodiode has a lower capacitance than the simple p-n junction. The PIN structure allows increasing the response speed without having leakage current since it is unnecessary to operate reverse biased.

The selected photodiode is made of Indium Gallium Arsenide, a semiconductor alike silicon, whose primary application is high-speed and highly sensitive photodiodes. Unlike silicon, this material is able to detect Near Infrared radiation. Besides the advantages this material presents, the photodiode is structured as a PIN junction that further increases its sensitivity and response speed without compromising signal quality.

As previously mentioned, a photodiode can be configured with two modes of operation: it can be either photovoltaic (unbiased) or photoconductive (reverse biased). In this case, the photodiode is configured to operate in photovoltaic mode since it is more crucial to have a lower noise and more linear output.

The photodiode generates a current that is necessary to be converted into an output voltage to extract the value obtained by the component. This conversion can be achieved with a transimpedance amplifier

(figure 3.22), a current to voltage converter capable of achieving high gain from a source with a low signal-to-noise ratio.
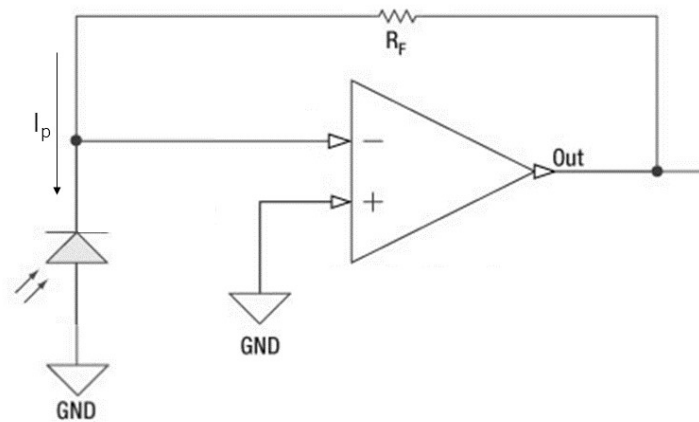

Figure 3.22: Simplified transimpedance amplifier

The inverting input of the operational amplifier has a very high impedance. For that reason, practically all of the current I_p generated by the photodiode is forced to run through the feedback resistor R_f. Since the amplifier's inputs are connected to ground, a voltage proportional to the current appears in the output of the amplifier. The feedback resistor defines the gain of the circuit, and the output voltage is a result of the current multiplied with the resistor value:

$$V_{out} = I_p * R_f \qquad (3.1)$$

Given that the selected gain for this stage was 1 million or 120dB, the feedback resistor has a value of 1MΩ.

In order for a transimpedance amplifier to operate correctly when paired with a photodiode, the selection of the operational amplifier is crucial. The operational amplifier selected to use on this application was the AD8066 [36] due to its low input offset voltage, low input bias current, very high input impedance and automotive certified. These characteristics are essential to retrieve appropriate information from the photodiode.

The simulation of the described circuit requires an implementation of a photodiode model. The photodiode is a component that generates a current, has high resistance and variable capacitance according to the bias voltage. Thus, it can be modelled as a current source in parallel with its shunt resistance and the corresponding capacitance to the applied voltage bias. In figure 3.23 is shown the model used in the simulations corresponding to the photodiode G12180-003A (from Hamamatsu).
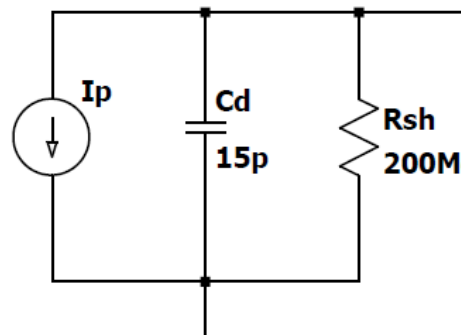
Figure 3.23: Photodiode model

In combination with the system's total capacitance, the feedback resistor creates a pole in the amplifier's loop transmission, resulting in instability. In figure 3.24 can be seen how the amplifier response becomes unstable after implementing the circuit of figure 3.22. The peaking effect and rapid phase shift are an indication of stability issues. The operational amplifier internal compensation is not able to stabilize its output with the addition of the external elements.
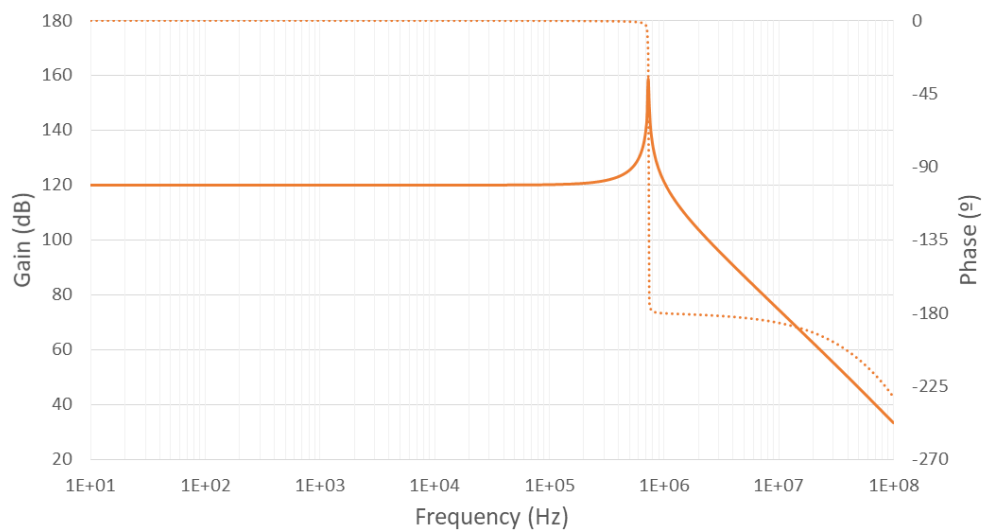
Figure 3.24: Bode diagram of transimpedance amplifier without compensation

The circuit needs a correction that allows operation without becoming unstable. To compensate for this instability, the addition of a zero in the feedback network (β) is necessary. This zero can be obtained using a capacitor in parallel with the feedback resistor, the feedback capacitor (C1 in figure 3.26). The value of the feedback capacitor is selected considering that the value of the zero is within the open-loop gain of the operational amplifier. This can be verified by comparing the noise gain with the open-loop gain. The zero corresponds to the frequency at which the noise gain curve stops increasing since a zero in the

β transfer function looks like a pole in the $1/\beta$ plot. If this point is inside the open-loop gain, the system is stable; otherwise, it is unstable. On the limit, this point can match the open-loop gain, maximizing the bandwidth of the system. This frequency is determined by the values of the feedback resistor and capacitor:

$$f = \frac{1}{2\pi R_f C_f} \tag{3.2}$$

Since the amplifier is expected to operate at a maximum frequency of 5kHz, the capacitor must not exceed 31.8pF. The selected capacitor has a capacitance of 22pF; thus, the zero is positioned at a frequency of approximately 7.2kHz. As shown in figure 3.25, the line corresponding to the noise gain stabilizes at the zero and is positioned within the amplifier's open-loop gain. This means that the requirements for stability are met.
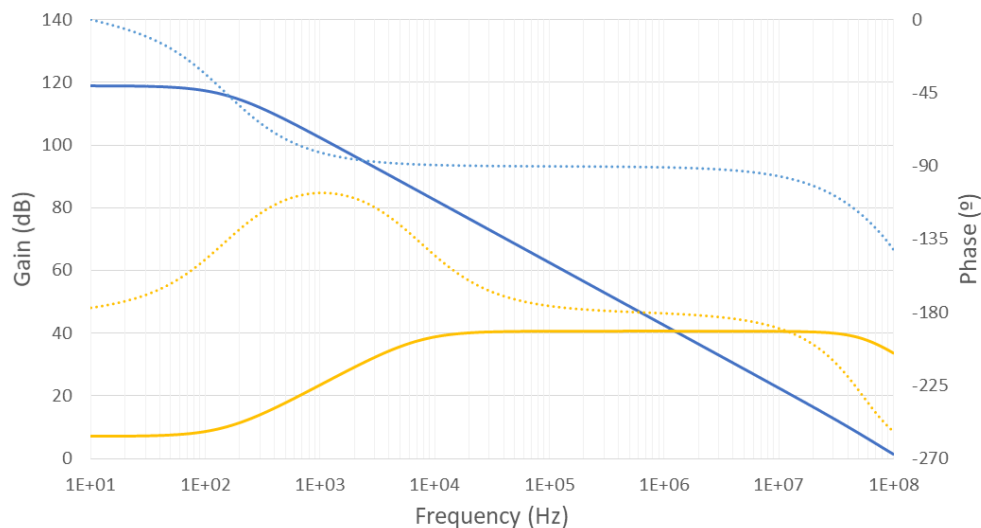
Figure 3.25: Bode diagram of open loop gain (blue) and noise gain (yellow) of AD8066

Besides the compensation previously described, matching the impedances at the inputs is also important. For that reason, the non inverting input must be connected to a resistor and capacitor (R4 and C2) with equal values to the ones on the feedback loop (C1 and R1). Matching the input terminal impedances eliminates common-mode noise peaking effects that increase the output noise. Besides that, the photodiode, amplifier and board parasitic capacitances must be taken into account and matched as well. Therefore capacitor C3 takes a value of 100pF that is enough to satisfy the sum of the referred capacitances.
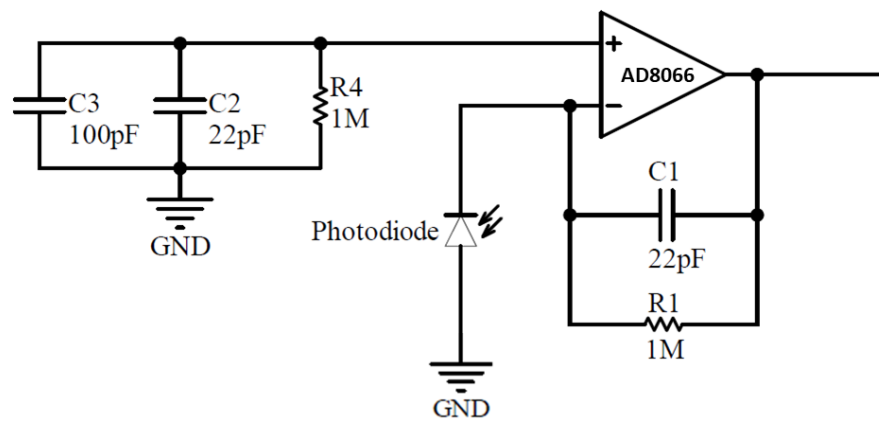
Figure 3.26: Complete transimpedance amplifier
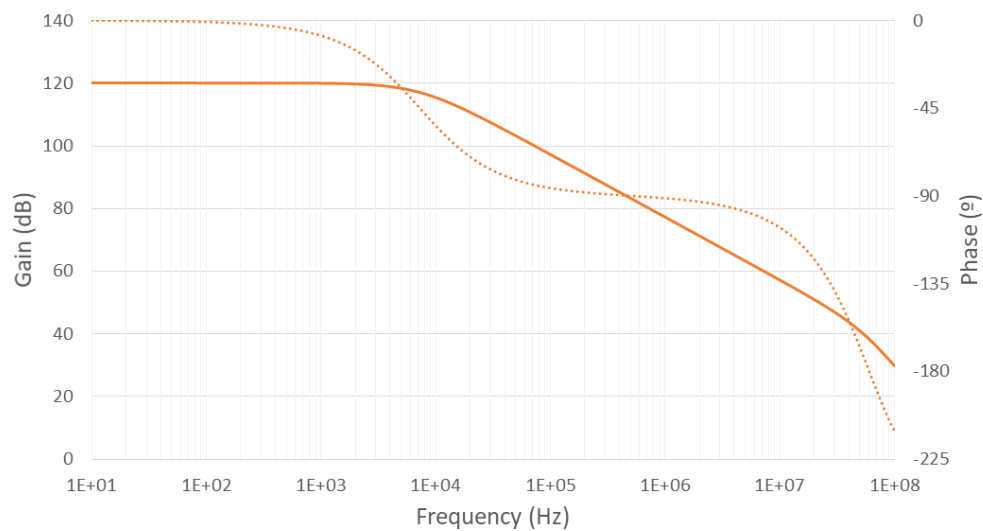
Figure 3.27: Bode diagram of compensated transimpedance amplifier

Even though the system is already amplified by 1 million, this is not enough. More amplification is required that was avoided to be done in a single stage, since a higher gain would result in a reduced bandwidth. For that reason a second stage was added in the form of a non-inverting operational amplifier (figure 3.28). For this stage was used the same operational amplifier as on the first stage. The bandwidth of the amplification circuit is limited by the first stage.
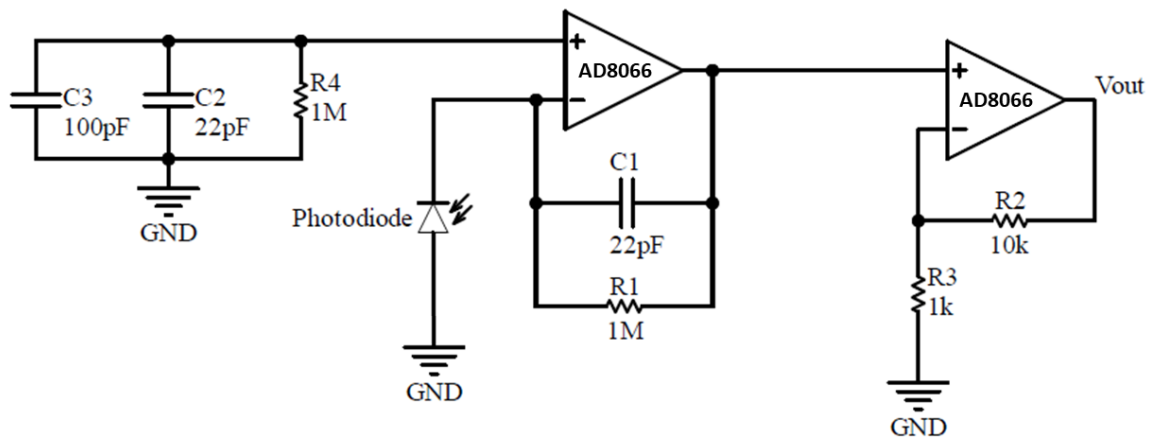
Figure 3.28: Circuit schematic of photodetector

The output of the first stage is connected to the non-inverting input of the second stage. This stage does not present stability problems so any special care is not necessary. A non inverting operational amplifier on the second stage has a gain that can be calculated as follows:

$$V_{out} = \left(1 + \frac{R2}{R3}\right) V_{in} \tag{3.3}$$

Therefore, the output of this stage is 11 times superior to the output of the first stage. The total gain of the circuit is the result of the multiplication of both gains, that is, the final gain is 11 million or approximately 141dB. In figure 3.29 is shown the Bode diagram of the complete amplification of the photodetector circuit.
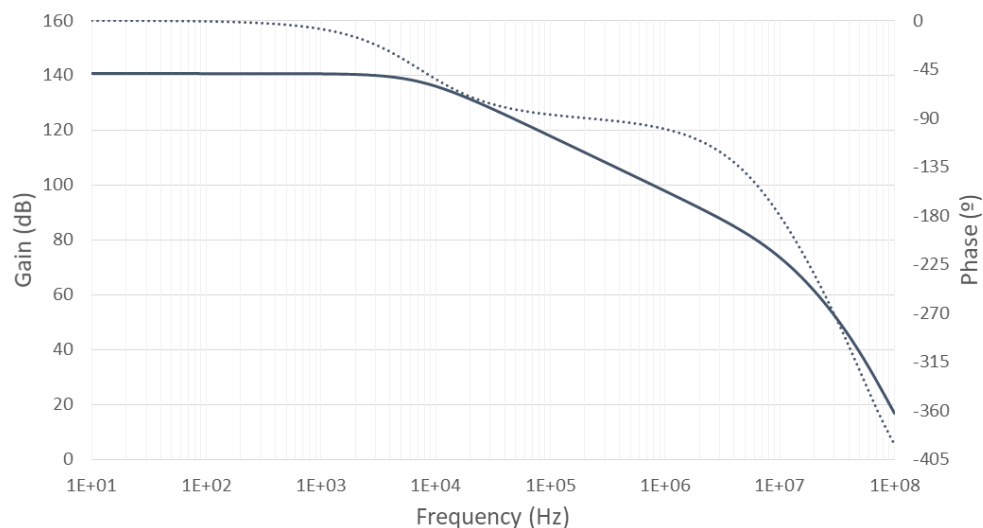
Figure 3.29: Bode diagram of final circuit

In figure 3.30, the PCB layout correspondent to the photodetector (figure 3.28) is shown.
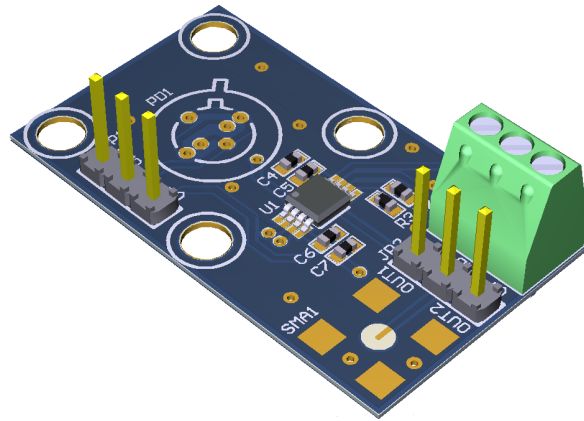
Figure 3.30: PCB layout of photodetector

3.4 Microcontroller
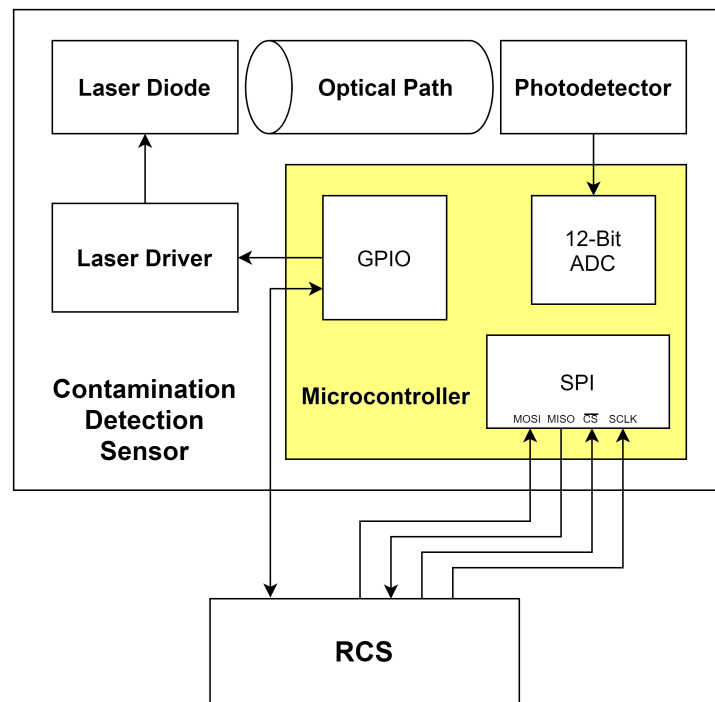
Figure 3.31: Microcontroller in the system architecture

The microcontroller is the element responsible for managing the laser and the data acquisition from the photodetector. Besides that, this element communicates with the RCS to synchronize and actuate at the right time, and to send information when necessary. The contamination detection sensor can be

activated by a request from the RCS via a GPIO pin and exchange information via SPI. The sensor emits an alarm through a GPIO pin whenever it desires to communicate with the RCS.

In this section, every aspect related to the microcontroller is described. Firstly, the RCS operation is briefly described in order to give information about when the Contamination Detection Sensor can operate and how both systems interact. Secondly, the description of the selected board and some hardware considerations are presented. Afterwards, the software is described.

### 3.4.1 Interaction with RCS

In order to gather the requirements of the contamination detection sensor, the typical operation of optical sensors must be known. Usually, these sensors use lasers to shoot some target and a photodetector to detect the reflected radiation. In the Road Condition Sensor case, a photodetector quantifies the intensity of reflected radiation shot by four different lasers. If the lasers were to be shot simultaneously, the intensity captured by the photodetector would be a sum of the four reflections. However, the system relies on the individual quantification of each reflection, so it demands to have dedicated time slots for each laser and correspondent detection. The RCS takes approximately 10ms to complete one cycle. The acquisition takes only 400μs and the remaining time is spent in the classifier (figure 3.32).
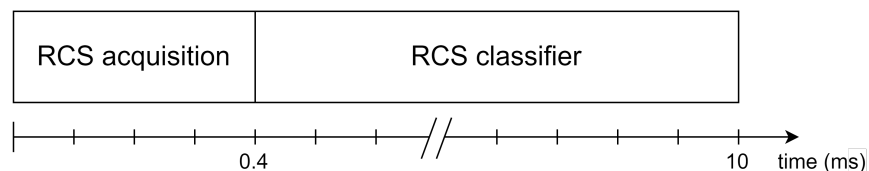
Figure 3.32: RCS operating time

The contamination detection sensor utilizes a laser diode that may interfere with the RCS detection capacity since radiation escaping from the window's interior can reach the photodetector of that system. For this reason, the contamination detection sensor must be activated outside the RCS acquisition time slot. Therefore, the sensor can operate in parallel with the RCS classifier, which means that it can take as long as 9.6ms. This solution completely eradicates any chance of affecting the performance of the primary system. Considering this, the sensor requires to be activated by a request from the primary system at any given time.

3.4.2 State diagram

The contamination detection sensor requires low software effort, given that the hardware takes care of most of the challenges. This means that the software is relatively simple.
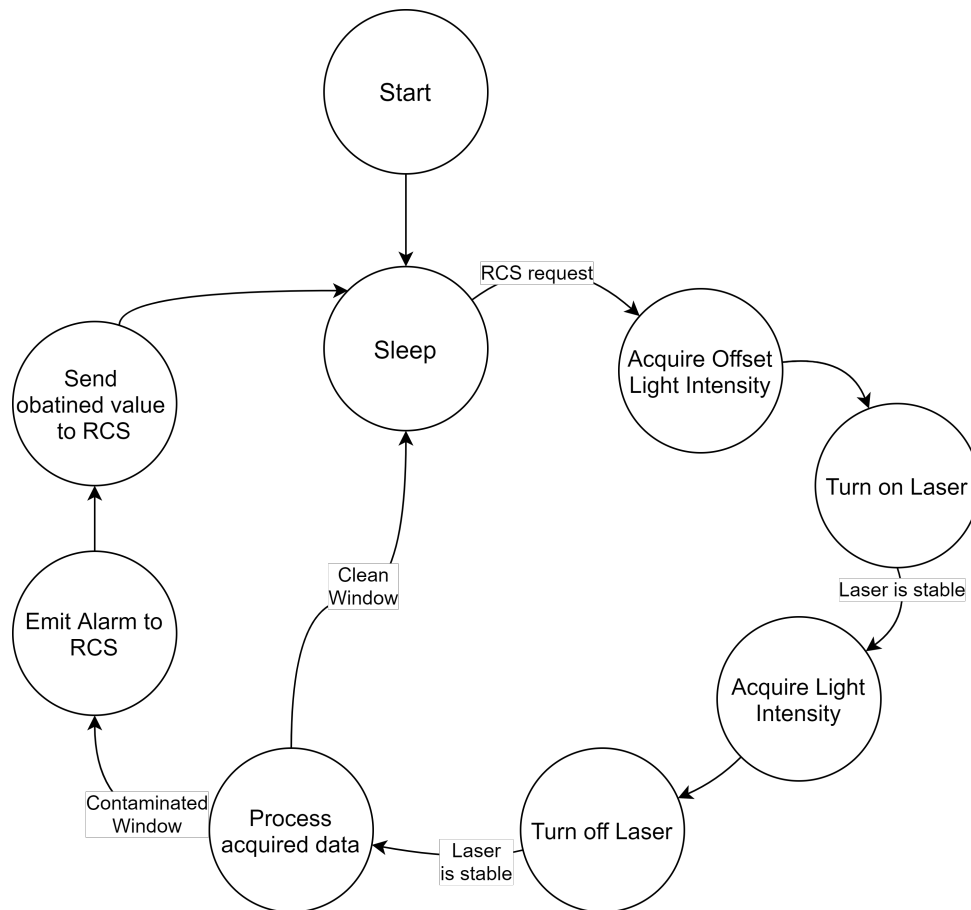
Figure 3.33: State diagram

The state diagram illustrates an overview of the software operation flow (figure 3.33). The system is waken up from sleep mode by an interrupt generated whenever the RCS makes a request. The contamination detection sensor starts by measuring the light intensity when the laser is turned off. It follows to retrieve the value when the laser is turned on and the acquired data is processed. The value is interpreted and, if it corresponds to a contaminated window, the system emits an alarm, sends the obtained value to the RCS and enters sleep mode. Otherwise the system enters sleep mode directly.

3.4.3   Sequence Diagram

The sequence diagram describes the interactions between the modules and the steps taken when the RCS requests the contamination detection sensor to operate. The sensor starts by acquiring the data from the photodetector when the laser is off. Then, the laser is activated. Once the laser is stable, the sensor acquires the data captured by the photodetector. After the reading is complete, the laser is turned off, and the system waits once again for stabilization. The retrieved data is processed, and if the sensor detects contamination, it emits an alarm and sends the value of detected light intensity to the RCS.
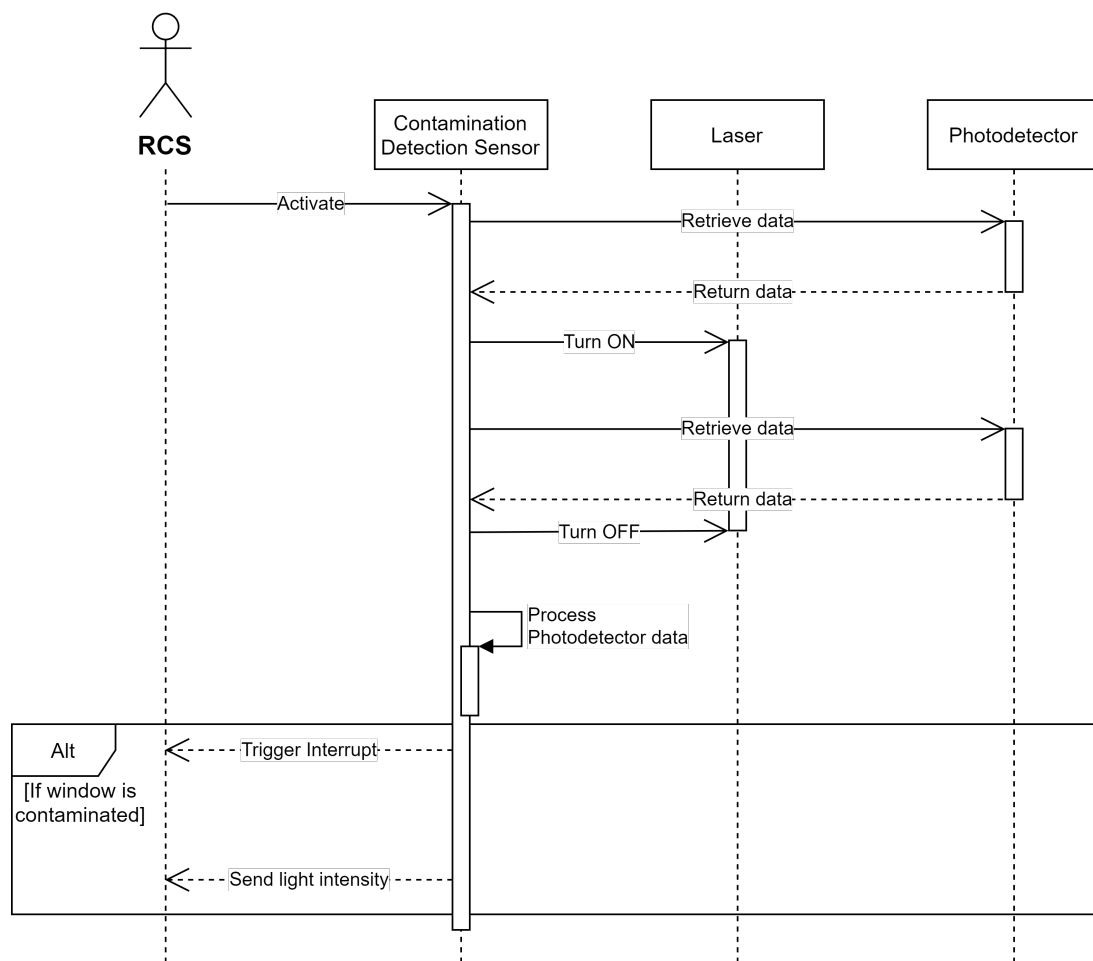
Figure 3.34: Sequence diagram

3.4.4   System stack

The system can be represented using layers. Starting from the bottom layer, the hardware consists in the selected NXP board. Above that, the Hardware Abstraction Layer, provided by S32 SDK (named

Peripheral Drivers), allows to interact with the hardware efficiently. With this basis layers, the processes of the application can be developed: GPIO manipulation, ADC conversion and SPI communication.
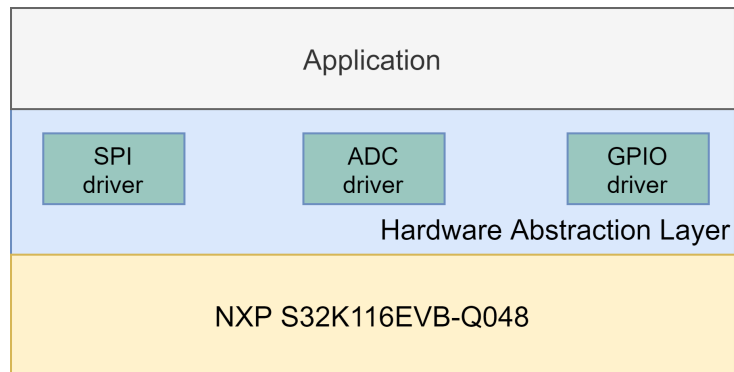
Figure 3.35: System stack

3.4.5 Hardware

The main requirements for the selection of the board are to have General Purpose Input/Output (GPIO) to control the laser, generate an interrupt in the RCS and be activated by the RCS; an Analog-to-Digital Converter (ADC) to translate the photodetector's output voltage into digital numbers and a Serial Port Interface (SPI) to communicate with the primary system. Since the sensor is for an automotive application, the board must comply with the safety standards accordingly.

Figure 3.36: NXP S32K116 evaluation board

For this proof of concept, the NXP S32K116EVB-Q048 was selected (figure 3.36), a low-cost evaluation and development board for general purpose automotive applications. Some of the main and relevant features for the application are:

- 32-bit Arm Cortex-M0+ core

- 12-bit Analog-to-Digital Converter

- Low Power Serial Peripheral Interface

- Headers with General Purpose Input/Output pins

For the developed application, the sensor requires 3 GPIO pins, 1 ADC channel and 4 pins for SPI communication. The used connections, the board pins and respective function are presented in table 3.1.

Table 3.1: Board pins

Connected to	Board Pin	Pin Function
Laser	PTB13	GPIO
Photodectetor	PTC1	ADC0_SE9
RCS CS	PTB5	LPSPI0_PCS
RCS MISO	PTB4	LPSPI0_SOUT
RCS MOSI	PTB3	LPSPI0_SIN
RCS SCLK	PTB2	LPSPI0_SCK
RCS Input pin	PTC8	GPIO
RCS Output pin	PTC9	GPIO

3.4.6 Sleep mode

Since the system only actuates when a request is made, there is no need to be continuously activated. For that reason, the board enters a sleep mode when there is nothing to execute.
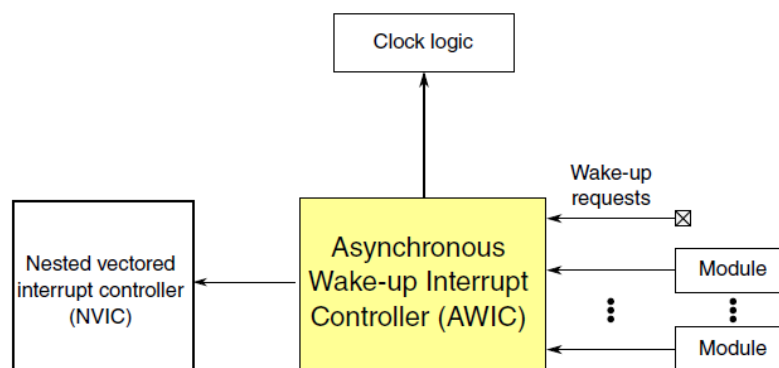

Figure 3.37: Asynchronous Wake-up Interrupt Controller [37]

The ARM Cortex M0+ core supports the power modes of Run, Sleep and DeepSleep. The S32K11x family provides multiple options within each power mode. The selected power mode for this application

was the Very Low Power Stop (VLPS) since it is the lowest power mode in which pin interrupts are still functional. The NVIC is disabled, so an Asynchronous Wakeup Interrupt Controller (AWIC) is used to wake the MCU (figure 3.37). The AWIC detects asynchronous wake-up events in stop modes and signals to clock control logic to resume system clocking. After clock restart, the NVIC observes the pending interrupt and performs the normal interrupt.

3.4.7 Flowcharts

In this section, the flowcharts of the implemented software are presented. Firstly, the interrupt service routine that wakes up the system is depicted. It is followed by the description of the main code and the data acquisition function (*GetCDSdata*).

The contamination detection sensor starts operating after an external interrupt is triggered by the RCS. The interrupt service routine is the first block being executed. It simply clears the relevant interrupt flag and sets the flag *Activated* (figure 3.38).
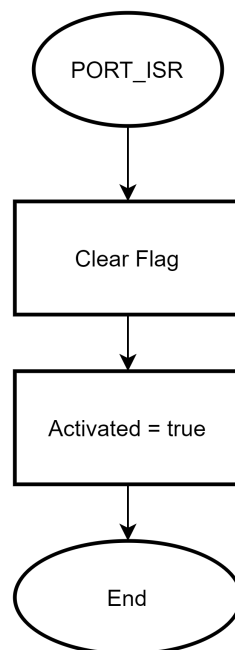
Figure 3.38: PORT_ISR flowchart

The main code of the system verifies if the flag *Activated* is set (figure 3.39). If so, it starts by entering the function *GetCDSdata*. The function returns the value of light intensity power. This value is compared with the range of values that correspond with a clean window. In case the acquired value is outside this range, the contamination sensor pulses the GPIO pin connected to the RCS to trigger an interrupt in that

system. This is followed by the transmission of the acquired value to the RCS via SPI. Afterwards, the system enters VLPS mode. In case the acquired value is within the range, the system goes instantly to sleep. At this point, execution is stopped and only restarts once an interrupt is triggered by the RCS.

In hindsight, the flag *Activated* is somewhat redundant since it is only expected to be tested when the RCS wakens up the system. However, it turns the software a bit more robust and makes it more versatile to new features.
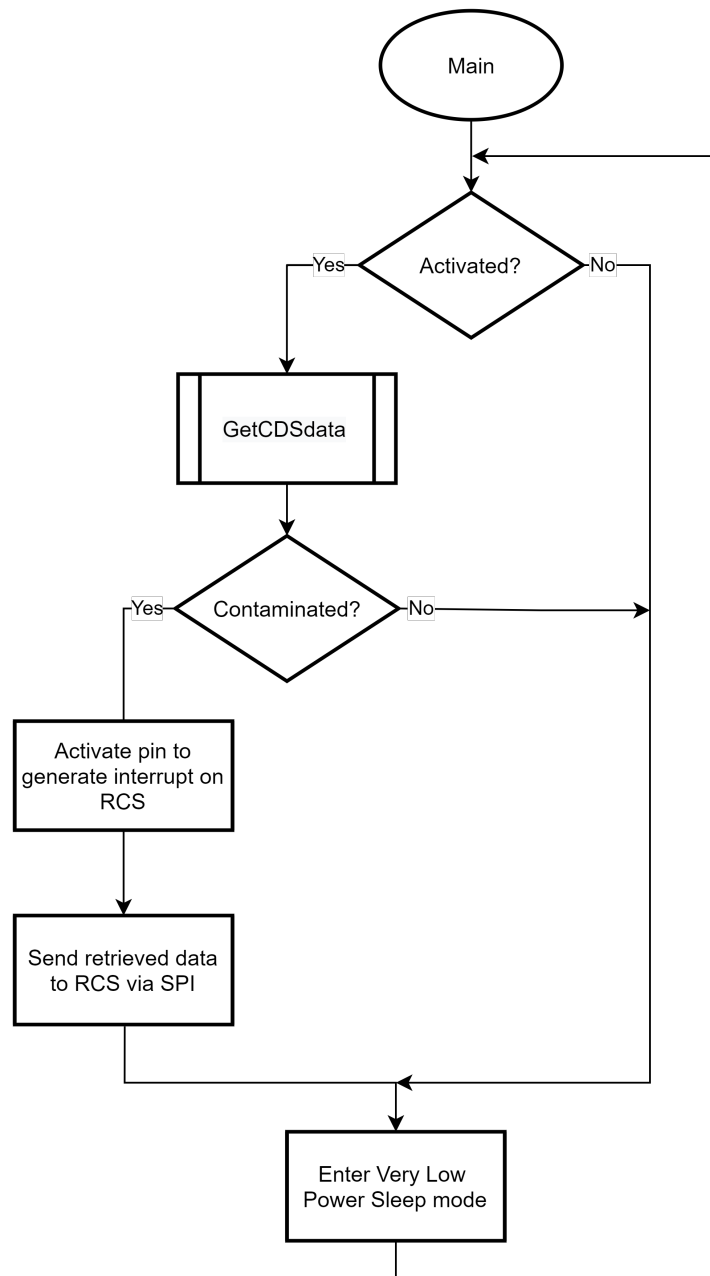
Figure 3.39: Main flowchart

The function *GetCDSdata* returns the light intensity reaching the photodiode (figure 3.40). It starts by

reading the value captured by the photodetector when the laser is turned off. Afterwards, the laser is turned on. The laser takes approximately 120µs to stabilize so it is necessary to wait for its stabilization. Later, it is read the photodetector value while the laser is turned on. The laser is turned off and, similarly to turning the laser on, there is also a stabilization time when turning it off. So, it waits for the stabilization in order to not interfere with RCS. By calculating the difference between the obtained values, some interferences can be ignored. The value is later converted to nanowatts (nW) taking into account the amplification gain and the photodiode sensitivity. Finally, the function returns the result.
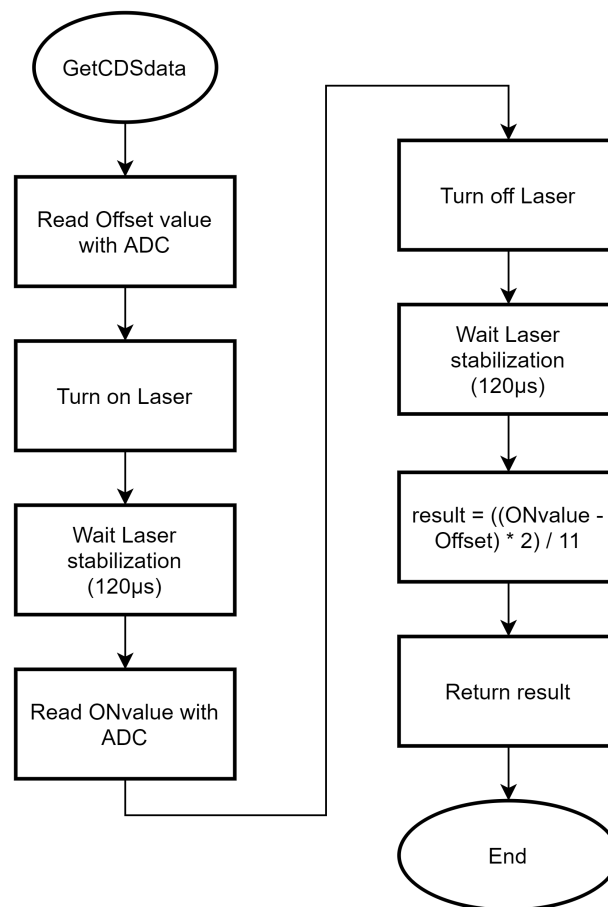
Figure 3.40: Flowchart of GetCDSdata function

3.5 Prototype
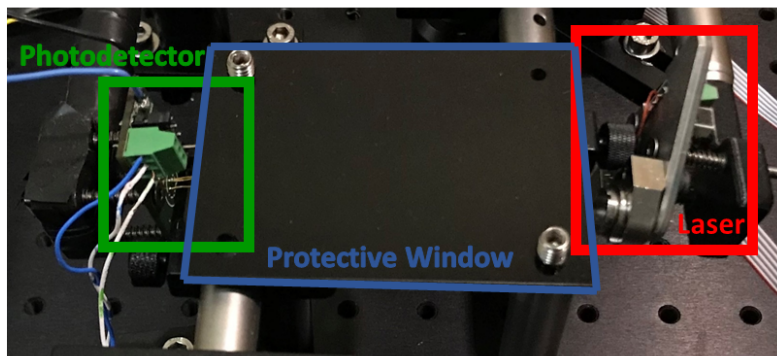
Figure 3.41: Prototype

The combination of the previous sections results in the prototype showed in figure 3.41. The laser board is positioned at the right end side and the photodetector board at the left end side. They are positioned according the description presented in 3.2.1 and 3.2.2. Although hidden beneath the window, the prisms are in front of the laser and the photodiode, glued to the window with the index matching gel.

In figure 3.42, the protective window was removed to demonstrate the laser, photodetector and prisms (with the index matching gel).
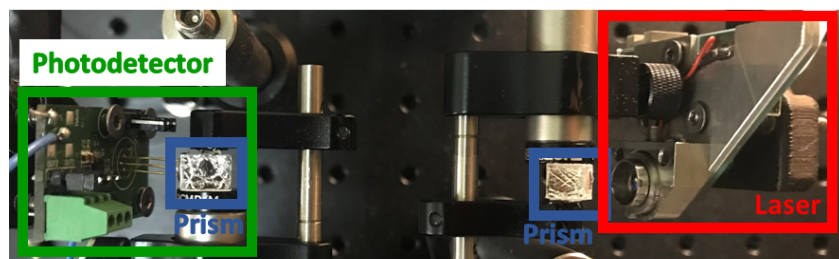
Figure 3.42: Prototype without protective window

Chapter 4

Results

Before advancing to assess the sensor described in the previous chapter, the application of omniphobic coatings, their characterization and selection was performed. The coating selection was the first step for a successful system since it repels the contaminants and prevents their adhesion. The following chapter starts by describing the coatings' application and discussing the results of their mechanical and optic characterizations. After, the results obtained with the contamination detection sensor prototype (figure 3.41) are presented and discussed. The chapter finishes with an analysis of the potential interference on the RCS caused by scattering.

4.1   Coatings Application

The coatings selection consists of a ceramic and a polymeric coating. The first one is the Cytonix LiquidGlass [38], a ceramic coating with hydrophobic and oleophobic properties whose primary application is repelling water, oil and dirt, with a focus on protecting car paint. The second one is the polymeric coating named Gentoo [39]. Gentoo is designed to repel water and most oils and solvents. This coating is advertised as being capable of preventing corrosion and adhesion of paint such as graffiti. It is an easy-cleaning coating able to withstand some abrasion.

The coatings were applied using the spin coating technique. Spin coating consists in a procedure to deposit uniform films onto flat substrates. The coating material is positioned on top of the substrate and rotated, creating a centrifugal force that spreads the material. This was the selected method to apply the coatings due to its easily controllable way of obtaining an even layer across the window with a thickness that can be controlled by simply adjusting the rotational speed.
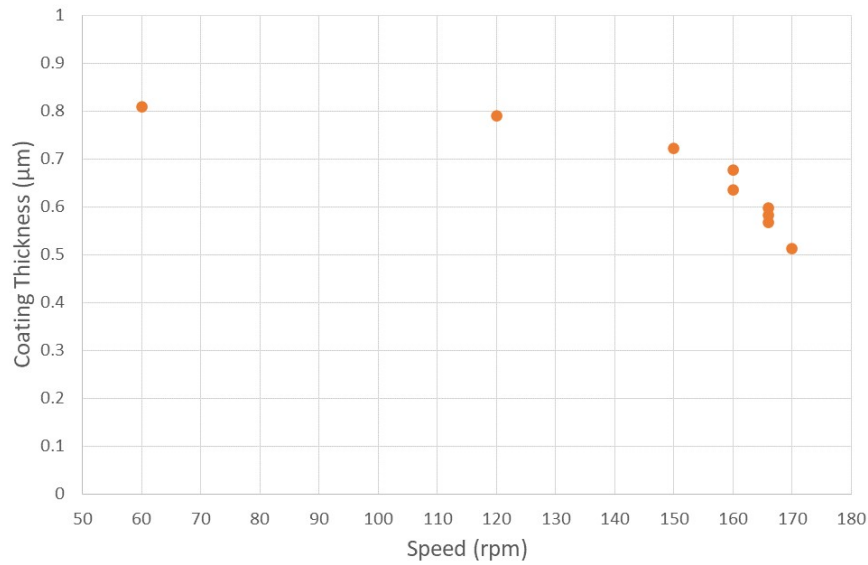
Figure 4.1: Cytonix Thickness

None of the coatings require or expect a spin coater; therefore, there is no information regarding the time and rotational speed to be used. Since the Cytonix is very fluid, it was decided to use the spin coater at a relatively low speed for an extended period of time. Gentoo is thicker; thus, the spin coater was configured with a broader range of speeds.

The application of the coatings was performed during 30 seconds (spin time). In the first 5 seconds, the top speed was programmed to be half of the selected one to ease into the desired rotational speed. After the 5 seconds and until the end of the deposition, the rotational speed is the desired and the one shown in figures 4.1 and 4.2.

Figure 4.2: Gentoo Thickness

Figure 4.1 and 4.2 represent the coating thickness as a function of the speed used on the spin coater for Cytonix and Gentoo, respectively. At a first instance, the spin coating deposition was performed at a wider range of speeds. After determining the best of those samples, this range was diminished in order to fine tune the samples. In figure 4.1 can be seen most of the fabricated samples. Meanwhile, in figure 4.2 is only shown the values retrieved at the second phase (due to the wider range used in the first step).

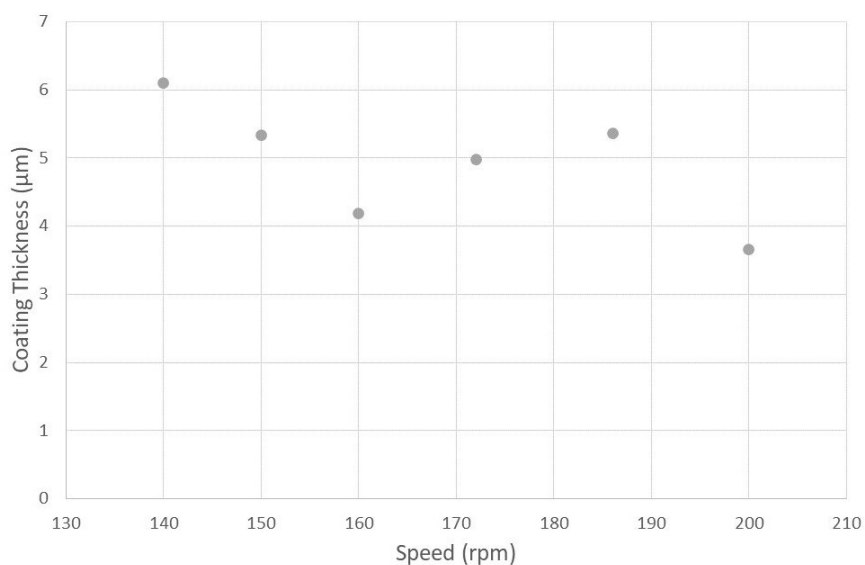In figure 4.1, the thickness of the Cytonix coating as a function of the speed used on the spin coater is depicted. This coating is very watery as can be confirmed with the resulting coating thickness. In figure 4.2, the thickness of the Gentoo coating in function of the speed used on the spin coater is presented. The thickness of this coating is greater than the Cytonix one. This is due to the difference in viscosity between them. Gentoo has a denser and stickier texture, and, for that reason, there is more build up on top of the substrate since it does not spread as much as the thinner coating. The best samples were determined by a Bosch team after realizing pollution tests and measuring the water contact angle. The thickness of Cytonix coating that presented best results was $\approx 0.6\mu$m, and the best thickness of Gentoo coating was $\approx 5.5\mu$m. These are the samples used and described in the following sections.

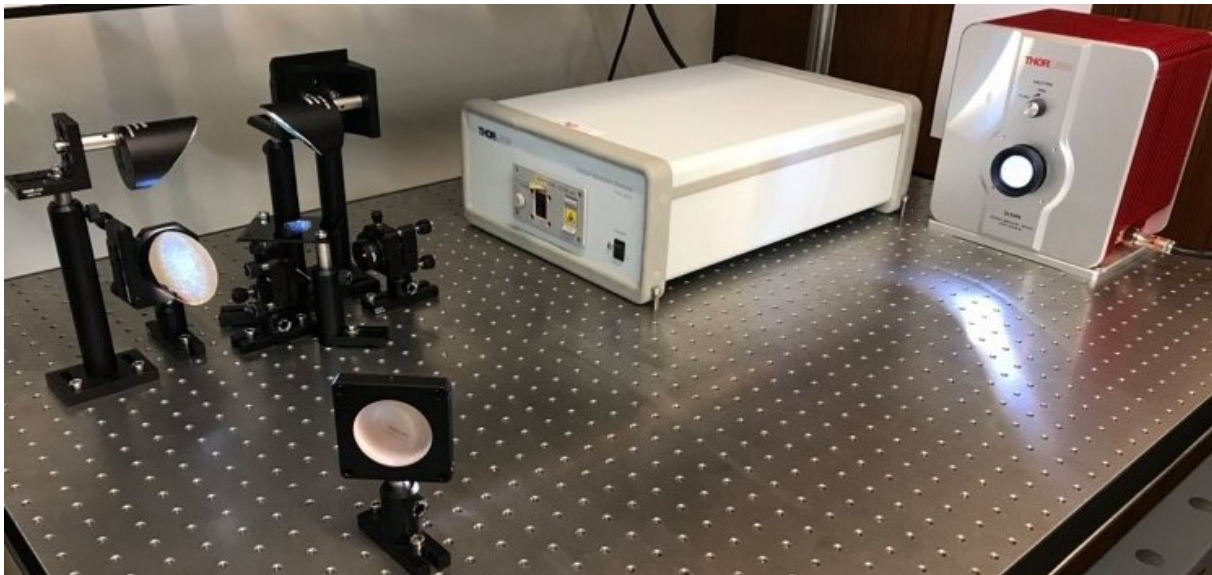## 4.2   Spectral Characterization

Figure 4.3: Setup for measuring transmittance.

In order to characterize the spectrometer properties of the samples, a setup involving a light source SLS401 [40] and an Optical Spectrum Analyzer OSA202C [41] were used. The source consists of a

xenon short-arc light that emits a collimated beam with spectral power distributed between 240nm and 2400nm. The Optical Spectrum Analyzer can perform accurate spectral measurements between 600nm and 1700nm. Thus, the following graphics range between these values. The range of values corresponds to near-infrared radiation, which contains the four relevant wavelengths to be studied for the application.

All materials have a signature transmission spectrum, and polycarbonate (the material of the window) is no exception. As shown in figure 4.4, certain wavelengths do not transmit through the window as much as the remaining. Wavelengths comprised between 1130nm and 1180nm, and between 1350nm and 1500nm present the typical lower value of transmittance for a material of this kind. The polycarbonate window also contains an optical filter that prevents the transmission of visible light. That is the reason why the transmittance is low on the initial values of the spectrum (600nm-730nm). Every other variation corresponds to the signature of the material that composes the window.
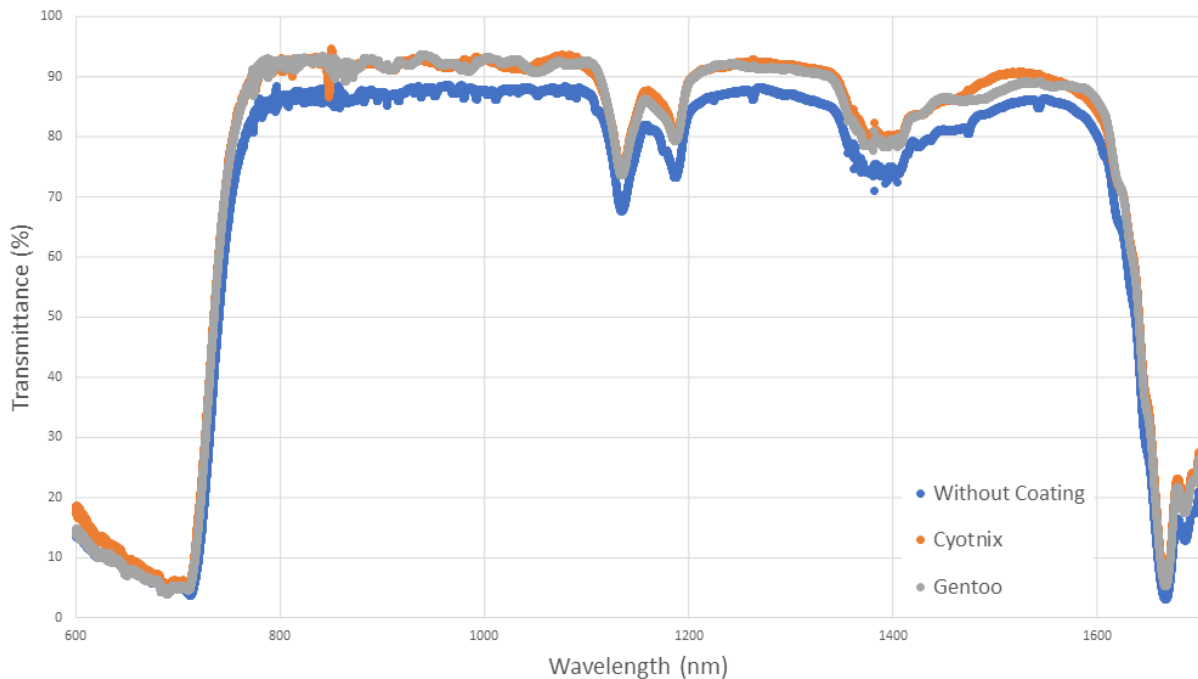
Figure 4.4: Transmittance of samples.

The spectral characterization of the uncoated and the coated samples are shown in figure 4.4. Both coated samples present a higher transmittance value than the uncoated sample throughout all analyzed wavelengths. This means that the coatings generate some anti-reflection effect. There are multiple ways of creating an anti-reflective coating, but the one that suits this situation is the index matching technique. This technique involves selecting a coating with a refractive index between the indices of the adjacent materials.

The existent interfaces on the uncoated and the coated samples are presented in figures 4.5 and 4.6, respectively. Although the angle of incidence represented on the figures is not parallel to the normal, on the following calculations, this angle is assumed to be $0°$.

The uncoated sample has only one interface between the air and the window. The transmittance and reflectance of this interface can be calculated via the Fresnel equations.

$$\mathcal{R} = 5.05\%$$

$$\mathcal{T} = 94.95\%$$
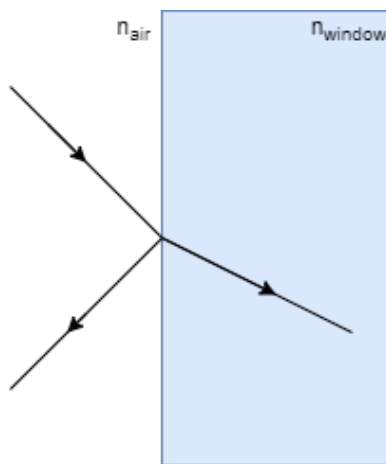
Figure 4.5: Interface of un-coated window.
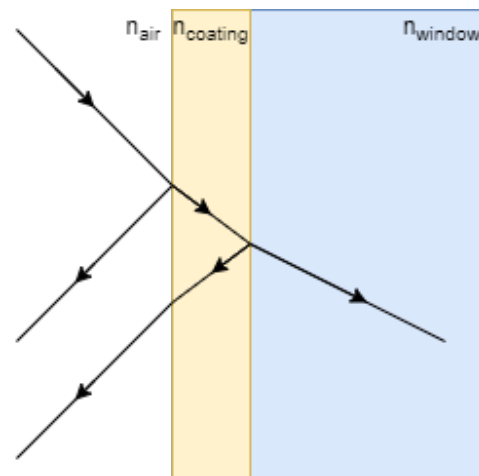
Figure 4.6: Interfaces of coated window.

The addition of the coating replaces the air to window interface with two interfaces: air to coating and coating to window. In case the coating has a refractive index value between the refractive indices of the polycarbonate window and the air, each of those interfaces exhibits less reflection than the original interface did. As an example, the refractive index of the coating is assumed to be 1.26. When calculated each interface's transmittance and reflectance, it is verified that the transmission on both interfaces is significantly higher than on the uncoated sample.

$$\mathcal{R}_1 = 1.32\%$$

$$\mathcal{T}_1 = 98.68\%$$

$$\mathcal{R}_2 = 1.27\%$$

$$\mathcal{T}_2 = 98.73\%$$

The overall transmittance between the air and the window corresponds to the multiplication of the transmittances calculated previously.

$$\mathcal{T}_{total} = 97.43\%$$

The value is considerably higher than the transmittance obtained on the uncoated version. This explains how applying a coating on a window can reduce its reflectance and, consequently, increase the transmittance. The selected value of refractive index is, in fact, the optimal value to obtain the highest transmittance possible.

$$n_{coating} = \sqrt{n_{air} n_{window}}$$

However, as long as the refractive index of the coating is comprised between the refractive indices of the surrounding materials, the transmittance will increase. In the case of the analyzed samples, the refractive indices of the coatings are unknown, but since the transmittance increased, the values must range between n_{air} and n_{window}.
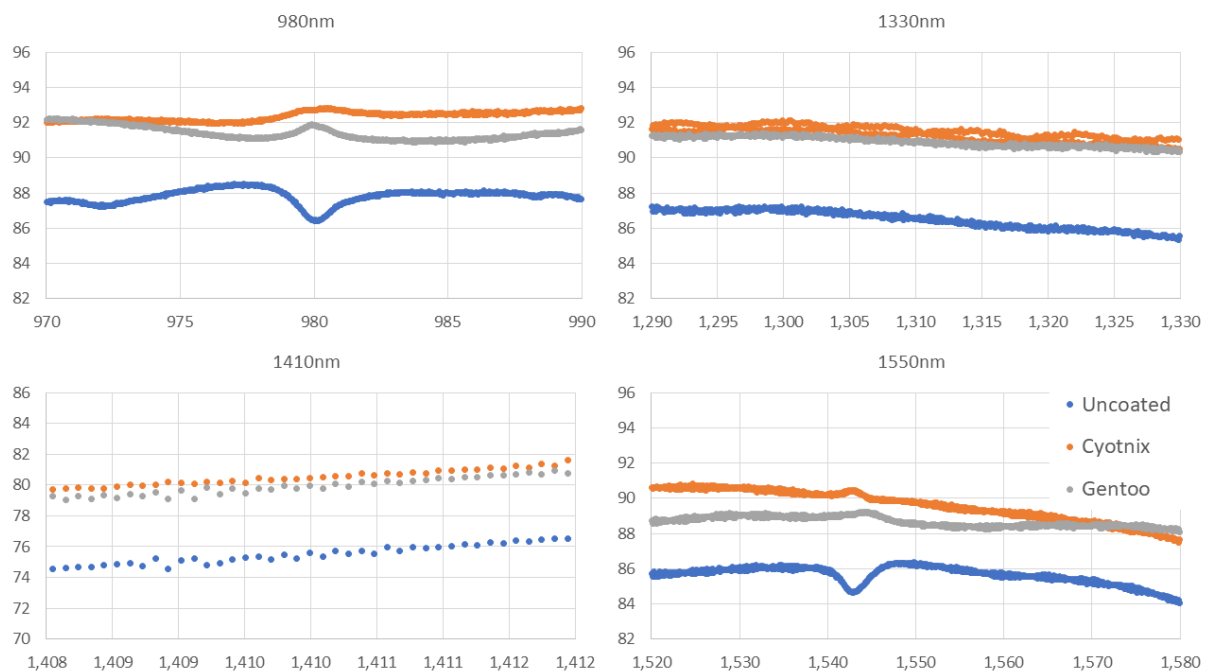

Figure 4.7: Transmittance of samples on the wavelengths of the RCS.

In figure 4.7, the same data as in figure 4.4 is presented, but with more focus and resolution on the wavelengths corresponding to the light sources used in RCS. Since the nominal wavelength of the lasers is not always the one that it actually emits, the range of wavelengths on each graph is comprised between the values that each laser can emit.

As shown in figure 4.4, both coated samples present higher transmittance than the uncoated sample and similar values throughout the spectrum. Further analysis demonstrates that the sample coated with Cytonix has a slightly higher transmittance on most of the four of the spectrum windows analyzed. However, the highest difference is around two percentage points compared to Gentoo. Since that is not a substantial difference, either coating is acceptable to be used on the system.

4.2.1 Contamination

Besides characterizing the spectral response of the window and coatings, the setup of figure 4.3 also allows to understand the mechanism of contamination. This characterization is relevant to relate the obtained values of the detection system with the amount of interference caused on the primary system.

In figure 4.8 is shown how much the transmittance varies with different quantity of water on top of the window. Water was placed on top of the window in a way that formed an uniform coating. The increase of water quantity means that the water thickness increases as well.
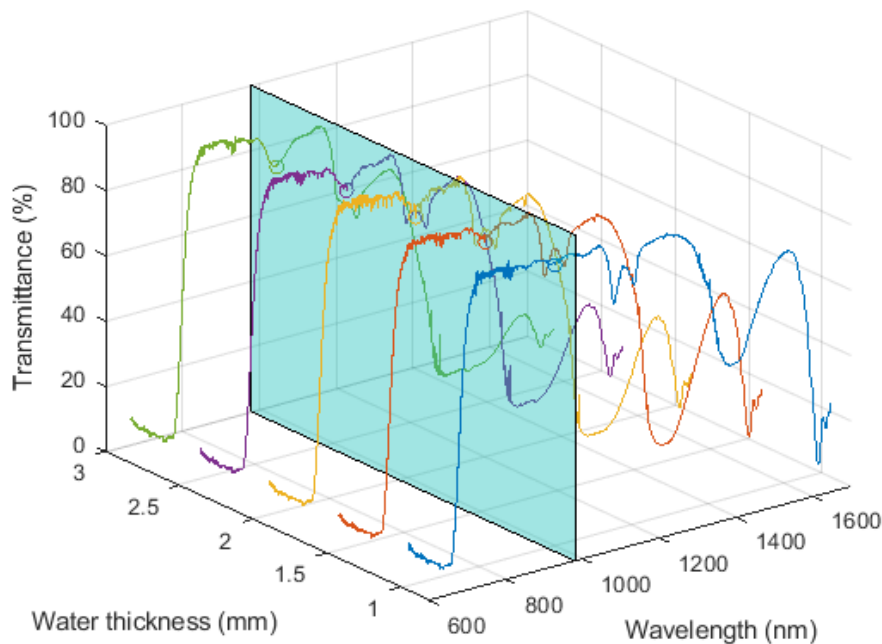

Figure 4.8: Water effect on transmittance

Overall, the transmittance through the window reduces with the increase of water thickness as expected. Water in liquid state absorbs near-infrared radiation mainly around the wavelengths 970nm, 1200nm, 1450nm and 1950nm, and heats up. As can be verified in figure 4.8, these are the wavelengths with the most noticeable variation. In figure 4.9 is shown the cross-section of the five graphs at a wavelength of 980nm (detection system laser wavelength). Similar to the complete spectrum, transmittance through the window decays as the contaminant quantity increases.
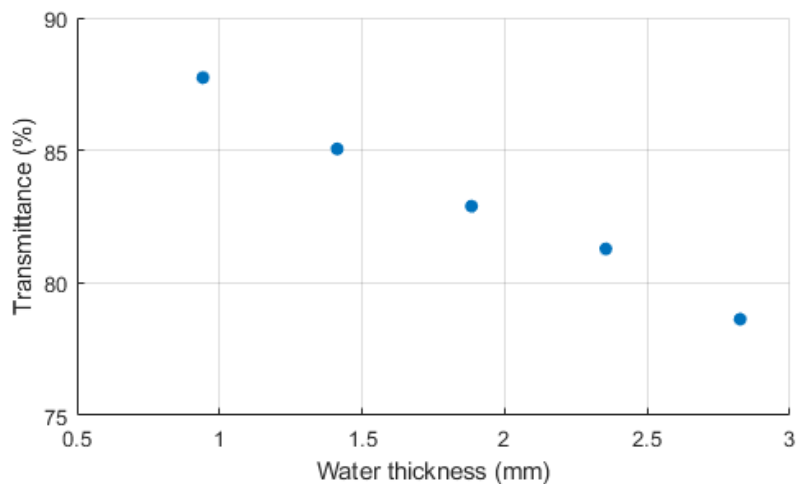
Figure 4.9: Water effect on transmittance at 980nm

In order for the system to identify a wide range of materials, a database containing the spectral characterization of these materials must be generated. Later, these characterizations have to be correlated with the detected values by the contamination detection sensor. These characterizations and respective correlation are out of the scope of this dissertation but an example is presented in section 4.3.1.

4.3   Detection system

The tests of contamination detection consisted of using the prototype to measure the radiation intensity that crosses through the window after spraying contaminants on top of the window. The prototype was set up with the window's outside face positioned to the top so the contaminants could be sprayed on it (figure 4.10).

The results obtained using the contamination detection system are presented in figures 4.11-4.13. Each spray corresponds to 0,55mL, and 15 sprays of each contaminant were applied on all samples. The contaminants used are the two most likely to pollute the window: diesel to simulate materials with oily properties and water.
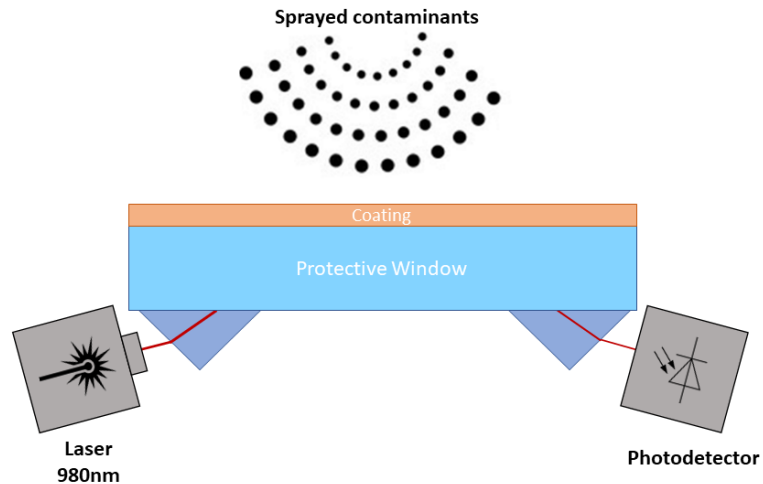
Figure 4.10: Prototype Setup

In figure 4.11, the measurements made using a window without any coating are depicted. When sprayed with water, there is an increase of radiation escaping the window's interior and, consequently, a decrease of light intensity captured by the photodetector. Power intensity reduces drastically after the first spray, and after the second one, it maintains around the same values. As it was being sprayed, it was visible that the spray quantity almost did not change the amount of water on top of the window since it did not stack up and drained. As for the diesel, the sprayed amount did not change the intensity of light travelling through the slab.
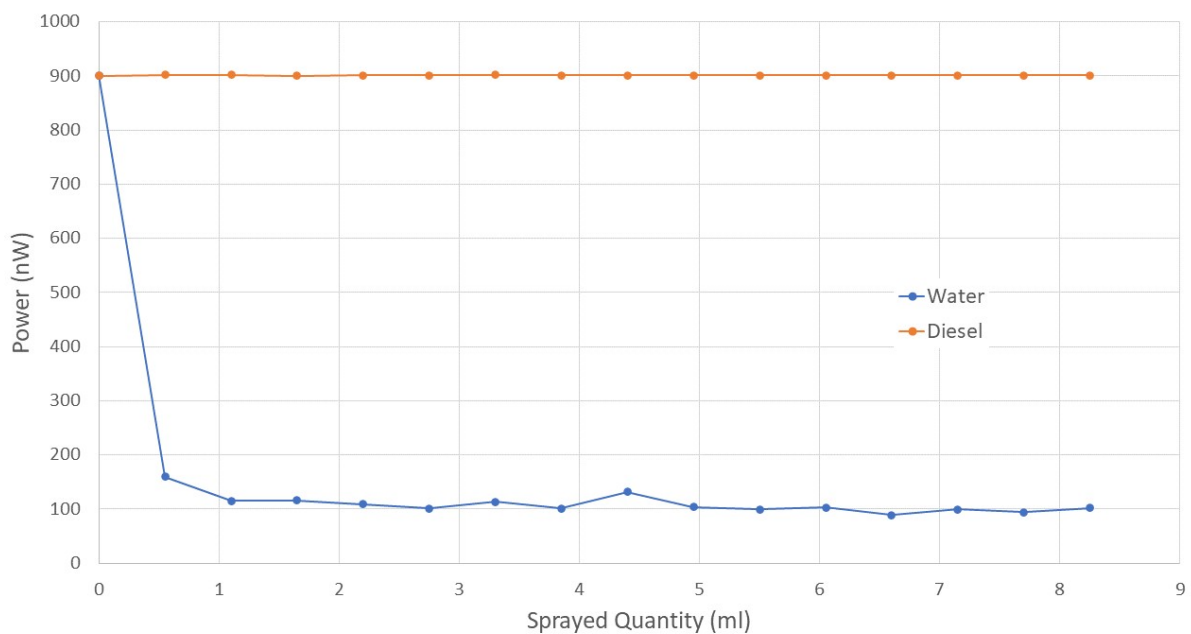
Figure 4.11: Prototype result Uncoated

The results obtained with a Cytonix coated window are demonstrated in figure 4.12. The water contamination effect on this sample is similar to the uncoated one, although with subtle differences. Unlike the uncoated results, the stabilization value is greater and it takes on more spray to reach it. The contamination with diesel presents a strange behaviour at first glance; the intensity of light drops substantially and after a few sprays returns to the uncontaminated value.

The tests using the window coated with Gentoo resulted in what is shown in figure 4.13. Similarly to the previous coated sample, water contamination increases the loss of radiation to the exterior of the window, and after the fourth spray the intensity stabilizes around a value inferior to the stabilization values of the other samples. As for the contamination with diesel, this sample presents a very different behaviour compared to the previous: the power of light detected by the photodetector decreases considerably, and the values oscillate a bit with every spray applied.
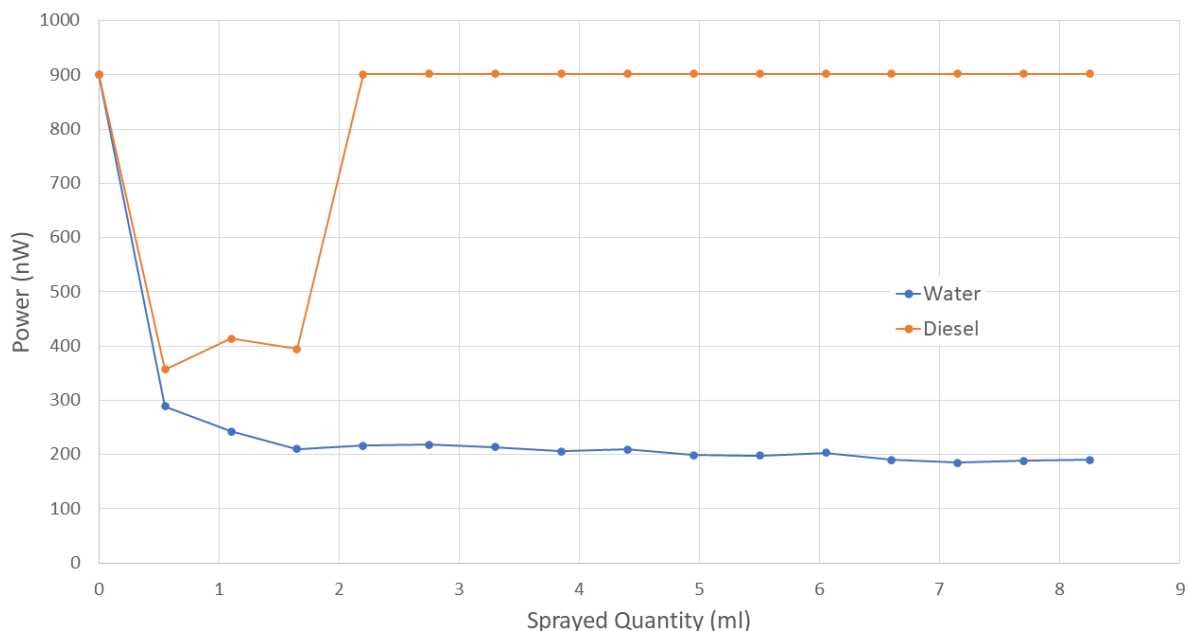
Figure 4.12: Prototype result Cytonix

Water contamination presents similar behaviour on all three samples. All of them stabilize after a few sprays since the water starts to drain when its quantity surpasses the amount that the surface tension can hold. The uncoated and coated samples can be differentiated by the number of sprays that require to stabilize. The coated samples require more water because the hydrophobic effect creates more tension than the uncoated, and it takes longer to start to drain since the water droplets stay perfectly in shape on top of the coating. When the droplet size reaches a specific size, they are drained and retain the same structure and water quantity. Gentoo coating takes one more spray than Cytonix, which can mean that the

polymeric coating has a more substantial hydrophobic effect. The three samples allow the identification of water very easily with the developed sensor.

Contamination with diesel is totally different: the results from each sample are quite distinct. In the test with the uncoated sample, diesel did not affect the intensity of light crossing the window. Diesel has a refractive index value very close to the window's value, and its low surface tension means that it easily couples to the window surface. Since it does not modify the refractive index of the system much, the intensity of light is not noticeably changed.

In the case of the Cytonix sample, the output oscillates significantly. This behaviour can be explained by the surface tension between the coating and the contaminant. At first, the coating presents sufficient tension to repel diesel. The contaminant stays above the contaminant, which in practice results in an average refractive index inferior to diesel; thus, its initial response is similar to the contamination with water. However, after a certain quantity, it can no longer retain the contaminant, and it couples with the coating. Diesel infiltrates on the coating, and since it has a similar refractive index as the window, its behaviour is comparable to the uncoated sample. At this point, diesel becomes a coating and eliminates the effect of Cytonix.
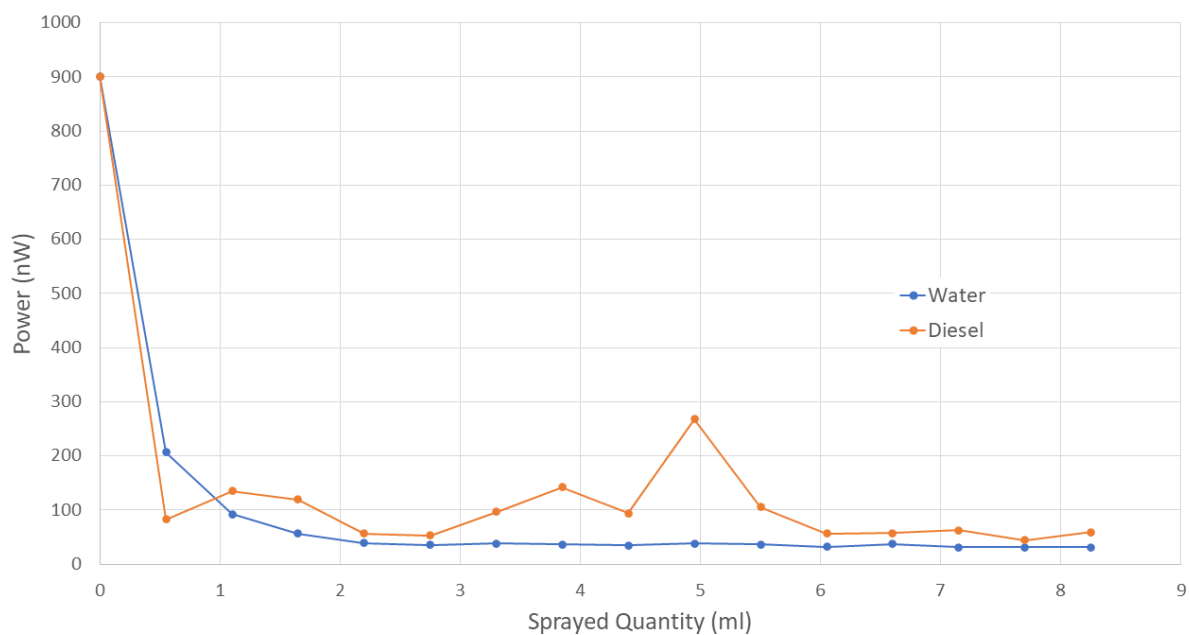

Figure 4.13: Prototype result Gentoo

With the Gentoo sample, the output is similar to the results obtained with water contamination, although with some oscillations. The oscillations are reasonably within a range, and it can be assumed that there is a stabilization after being contaminated. Unlike the Cytonix, this coating can retain sufficient

surface tension and repel diesel independently of its quantity. This behaviour shows that Gentoo presents a greater capacity of lipophobicity compared to Cytonix.

Overall, Gentoo coating presents the best results due to its capability of repelling both water and hydrocarbons successfully and the ability of this coating to turn possible the identification of a surface uncontaminated, contaminated with water and with diesel.

4.3.1   Relation with transmittance

In section 4.2.1, the effect of water contamination on the transmittance of the window is presented. Those spectral characterizations and the detection system results can be combined to obtain a relation between the sensor output and the interference on the transmittance. The relation shown in figure 4.14 corresponds to an approximation since the spectral characterizations are of uniform coatings of water, and in the contamination detection tests, the water was in the form of droplets. However, the droplets can be translated to an average water thickness. It is possible to correlate transmittance and sensor output taking the water quantity applied in each occasion as an intermediary.
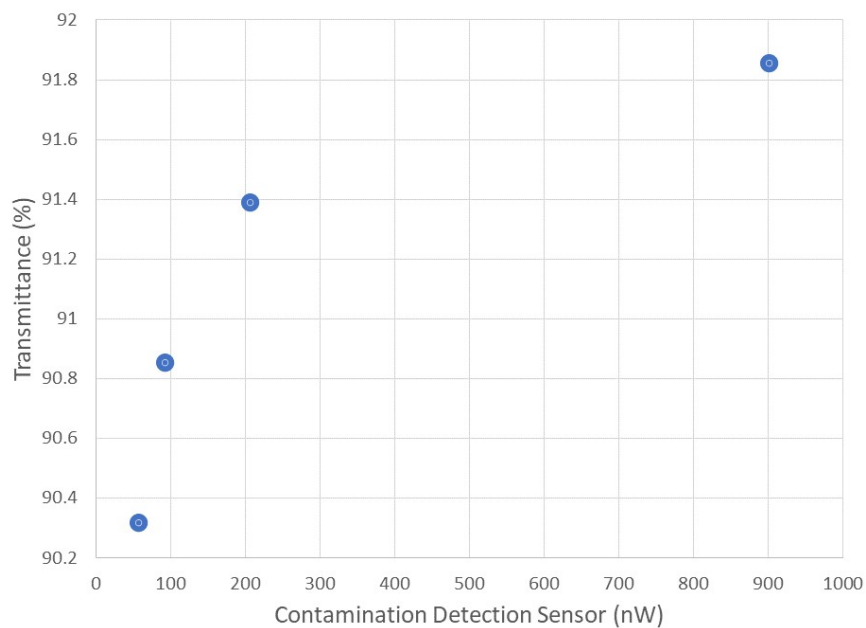

Figure 4.14: Sensor output vs Transmittance

The points used in this relation are the first four of figure 4.13 since these are the ones that are still possible to verify any variation. After these points, the sprayed quantity on the window does not correspond to an increase in water thickness, given that it starts to drain.

4.4   Scattering quantification

Light scattering is the change of direction of electromagnetic radiation due to a collision with some particle. The transmission, reflection, and refraction processes are macroscopic manifestations of scattering occurring on a submicroscopic level [10]. As explained in the Huygens' principle, light propagates as wavefronts. Every point on a wavefront is the source of spherical wavelets, and the secondary wavelets emanating from different points mutually interfere. The sum of these spherical wavelets forms a "new" wavefront. Points in different media result in spherical wavelets with different speeds. The speed difference modifies the resulting wavefront into another shape and direction.

The window's structure can present unknown impurities, such as air bubbles, that can moddify the wavefronts and, consequently, cause radiation to scatter out of the window. This radiation could potentially interfere with the Road Condition Sensor, so it is essential to quantify it.
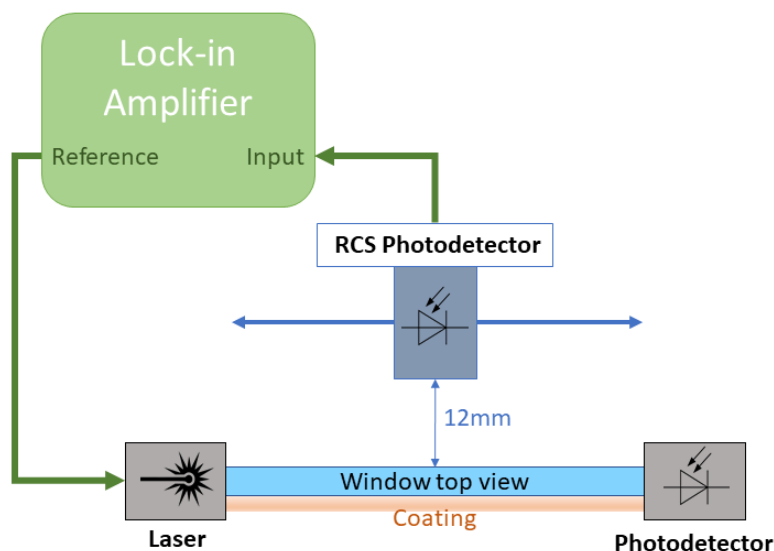
Figure 4.15: Setup for scattering measurement

The setup to measure scatter consists of the contamination detection sensor's laser and the RCS's photodetector as depicted in figure 4.15. The laser is positioned so that the angle of incidence is superior to the critical angle, and the photodetector is positioned behind the window at a distance of 12 millimetres mounted on a stage that allows moving along the length of the window (figure 4.15). The laser of the contamination detection sensor and the RCS's photodetector are connected to a lock-in amplifier in order to be possible to capture a very low amplitude signal correspondent to scattered radiation, as explained in section 2.2. The laser emits radiation with reference signal's properties and it travels through the window.

This signal is captured by the photodiode and, after amplification and filtering (as explained in section 3.3.2), it is then fed as the input signal of the lock-in amplifier.

Figure 4.16: Scattering

In figure 4.16 is shown the results that characterize the scattering present along the window samples. The three samples present very similar scattering through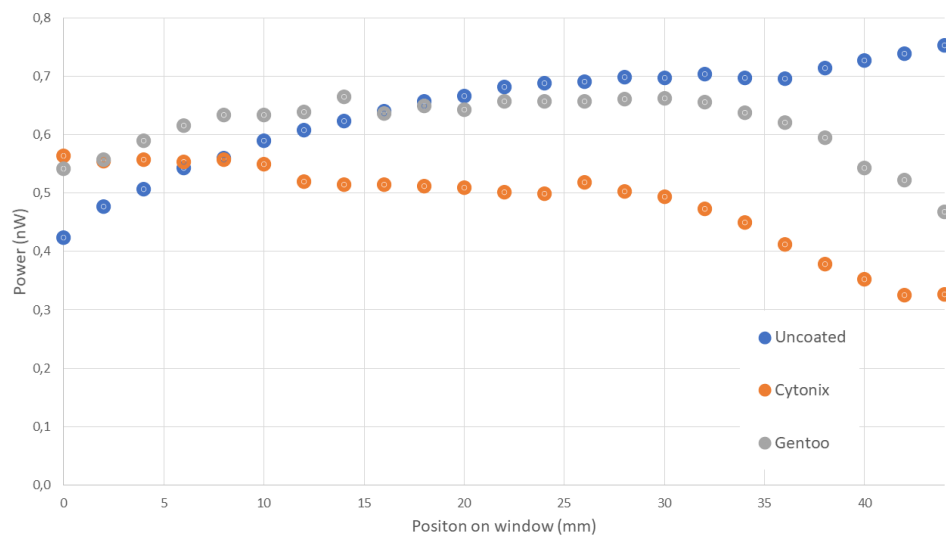out the window with only small differences. The detected intensity can be considered negligible since the interference values range between approximately 0.03% and 0.08% of the total power that the photodetector can detect.

Chapter 5

Conclusion

This dissertation proposed a solution to minimize the impact and identify the presence of contaminants on the protective window of the RCS (optical sensor).

Firstly, in order to minimize contamination, coatings capable of repelling water and oils were applied to the protective window. These coatings must perform their function without compromising the performance of the RCS, meaning that the coating must be "invisible" to the sensor. For that reason, after applying the coatings, a spectral characterization was made to study the influence of the coating on the window's transmittance. This characterization showed that the coatings actually increased the transmittance over all wavelengths (figure 4.4). With this in mind, both coatings were considered appropriated to be used as contaminant repellent since they do not affect the optical sensor's performance.

Secondly, the contamination was also characterized, following the same methodology used for the coatings. This analysis allowed to determine how the transmittance is affected by contaminants and later compare the results obtained with the developed prototype. The transmittance reduces with the increase of water thickness, as depicted in figure 4.8.

Finally, the prototype was tested with the primary objective of identifying contamination. As can be verified in figures 4.11, 4.12, and 4.13, water can be easily identified in any window sample (without coating, and with Cytonix and with Gentoo coatings). However diesel can only be successfully detected using the Gentoo coating due to its excellent capability of repelling oils and water. The uncoated version only allows to detect water, and the sample with Cytonix can present misleading results when contaminated with diesel. The conclusion made above implies that the contamination detection sensor operates correctly.

In addition, the scattering study allowed quantifying how much the sensor can influence the RCS via this type of loss. The obtained results show that scattering is basically negligible and, consequently, the interference due to scattering is insignificant.

The developed sensor meets all the requirements and presents a feasible solution for monitoring contamination on the protective window of the RCS. Possibly, it can be adapted to operate with other optical sensors.

5.1   Future work

This section highlights the aspects for improvement and future work. The main point for future work is to realize extensive testing to generate a calibration algorithm according to the contamination. This calibration algorithm will allow the main sensor to adapt and correct its own readings. To achieve that, a vast characterization of the influence of each contaminant on the window's transmittance is necessary. Along with that, a characterization of the same contaminants must be made with the contamination detection sensor. The crossover of these characterizations results in a dataset that can be used to obtain an identification model.

Apart from that, the contamination detection sensor has to be integrated within the Road Condition Sensor: from the physical integration of the hardware in the same package to the software described in this thesis and the identification algorithm.

References

[1] D. Altavilla, "NVIDIA And Mercedes-Benz Join Forces In An Autonomous Car Power Play." `https://www.forbes.com/sites/davealtavilla/2020/06/23/nvidia-and-mercedes-benz-join-forces-in-an-autonomous-car-power-play/`, 2020. (Accessed on 02-08-2021).

[2] A. Grzywaczewski, "Training AI for Self-Driving Vehicles: the Challenge of Scale | NVIDIA Developer Blog." `https://devblogs.nvidia.com/training-self-driving-vehicles-challenge-scale/`, 2017. (Accessed on 02-08-2021).

[3] D. Grannan, "'Human-like vision' pivotal to unlocking autonomous driving." `https://www.automotiveworld.com/articles/human-like-vision-pivotal-to-unlocking-autonomous-driving/`, 2020. (Accessed on 03-08-2021).

[4] W. J. Fleming, "New automotive sensors—a review," *IEEE Sensors Journal*, vol. 8, no. 11, pp. 1900–1921, 2008.

[5] M. Parker, "Automotive radar," in *Digital Signal Processing 101*, pp. 253–276, Newnes, second edition ed., 2017.

[6] Y. Li and J. Ibanez-Guzman, "Lidar for autonomous driving: The principles, challenges, and trends for automotive lidar and perception systems," *IEEE Signal Processing Magazine*, vol. 37, no. 4, pp. 50–61, 2020.

[7] A. T. Chen, N. D. Abe, C. R. Mullen, and C. C. Gilbert, "Contamination Sensitivity And Control Of Optical Sensors," in *Optical Systems Contamination: Effects, Measurement, Control* (A. P. M. Glassford, ed.), vol. 0777, pp. 97 – 126, International Society for Optics and Photonics, SPIE, 1987.

[8] M. P. Keating, *Geometric, physical, and visual optics*. Elsevier Health Sciences, 1988.

 [9] G. Duree Jr, "Geometrical Optics: Working with More Than One Ray," in *Optics For Dummies*, p. 58, Wiley Publishing, Inc., 2011.

[10] E. Hecht, "The Propagation of Light," in *Optics*, pp. 86–106, Addision Wesley, 4th ed., 2002.

[11] A. I. Vistnes, *Reflection, Transmission and Polarization*. 2018.

[12] E. Hecht, "Reflection," in *Optics*, pp. 95–100, Addision Wesley, 4th ed., 2002.

[13] E. Hecht, "Refraction," in *Optics*, pp. 100–106, Addision Wesley, 4th ed., 2002.

[14] G. Duree Jr, "Bouncing light back with refraction: Total internal reflection," in *Optics For Dummies*, pp. 52–53, Wiley Publishing, Inc., 2011.

[15] R. Paschotta, "Ray Transfer Matrix." `https://www.rp-photonics.com/abcd_matrix.html`. (Accessed on 14-09-2021).

[16] R. Paschotta, "Paraxial Approximation." `https://www.rp-photonics.com/paraxial_approximation.html`. (Accessed on 14-09-2021).

[17] D. F. Swinehart, "The beer-lambert law," *Journal of chemical education*, vol. 39, no. 7, p. 333, 1962.

[18] G. Duree Jr, "Calculating Reflected and Transmitted Light with Fresnel Equations," in *Optics For Dummies*, pp. 131–141, Wiley Publishing, Inc., 2011.

[19] J. Krepelka, "Maximally flat antireflection coatings," *Jemná Mechanika A Optika*, vol. 3, no. 5, pp. 53–56, 1992.

[20] A. Taflove and S. C. Hagness, *Computational Electrodynamics: The finite-difference time-domain method*. Artech House, 3rd ed., 2005.

[21] O. Romanov and A. Tolstik, "Finite-Difference Time-Domain Simulation of Light Propagation in 2D Scattering Media," no. 3, 2009.

[22] D. M. Sullivan, *Electromagnetic simulation using the FDTD method*. IEEE Press, 2000.

[23] Zurich Instruments, "Principles of lock-in detection and the state of the art," 2016.

[24] "50 MHz Lock-in Amplifier | Zurich Instruments." `https://www.zhinst.com/europe/en/products/hf2li-lock-in-amplifier`. (Accessed on 08-10-2021).

[25] L. Oberli, D. Caruso, C. Hall, M. Fabretto, P. J. Murphy, and D. Evans, "Condensation and freezing of droplets on superhydrophobic surfaces," aug 2014.

[26] A. Tuteja, W. Choi, J. M. Mabry, G. H. McKinley, and R. E. Cohen, "Robust omniphobic surfaces," *Proceedings of the National Academy of Sciences of the United States of America*, vol. 105, no. 47, pp. 18200–18205, 2008.

[27] H. J. Dutton, *Understanding optical communications*, vol. 1. Prentice Hall PTR Durham, North Carolina, USA, 1998.

[28] "Rain sensor and headlight sensor testing | HELLA." `https://www.hella.com/techworld/au/Technical/Car-electronics-and-electrics/Check-change-rain-sensor-42078/`. (Accessed on 03-12-2020).

[29] Newport, "Laser Diode Technology and Applications." `https://www.newport.com/t/laser-diode-technology`, 2013. (Accessed on 15-06-2021).

[30] "Thorlabs - L980P010 980 nm, 10 mW, Ø5.6 mm, A Pin Code, Laser Diode." `https://www.thorlabs.com/thorproduct.cfm?partnumber=L980P010`. (Accessed on 02-08-2021).

[31] G. Duree Jr, "Looking at Lenses: Two Refracting Surfaces Stuck Close Together," in *Optics For Dummies*, pp. 91–92, Wiley Publishing, Inc., 2011.

[32] Edmund Optics, "All About Aspheric Lenses." `https://www.edmundoptics.eu/knowledge-center/application-notes/optics/all-about-aspheric-lenses/`, 2013. (Accessed on 10-08-2021).

[33] R. Paschotta, "Numerical Aperture." `https://www.rp-photonics.com/numerical_aperture.html`. (Accessed on 10-08-2021).

[34] "InGaAs PIN photodiode G12180-003A | Hamamatsu Photonics." `https://www.hamamatsu.com/eu/en/product/type/G12180-003A/index.html`. (Accessed on 02-08-2021).

[35] Hamamatsu, "Si photodiodes handbook," 2020.

[36] "AD8066 Datasheet and Product Info | Analog Devices." `https://www.analog.com/en/products/ad8066.html`. (Accessed on 20-05-2021).

[37] NXP, "S32K1xx Series Reference Manual," 2018.

[38] "Cytonix LiquidGlass DTO5." `https://www.cytonix.com/LiquidGlass-DTO-p/dto_5_125ml.htm`. (Accessed on 08-10-2021).

[39] "Gentoo™ Anti-Corrosion & Easy-Cleaning Coating." `https://spillcontainment.com/products/gentoo-anti-corrosion-easy-cleaning-coating/`. (Accessed on 08-10-2021).

[40] "Thorlabs - SLS401 Xenon Short-Arc Light Source with Control Unit, 240 - 2400 nm." `https://www.thorlabs.com/thorproduct.cfm?partnumber=SLS401`. (Accessed on 08-10-2021).

[41] "Thorlabs - OSA202C Fourier Transform Optical Spectrum Analyzer, 600 - 1700 nm." `https://www.thorlabs.com/thorproduct.cfm?partnumber=OSA202C`. (Accessed on 08-10-2021).